Author Name

Book title goes here

Foreward

I am delighted to introduce the first book on Multimedia Data Mining. When I came to know about this book project undertaken by two of the most active young researchers in the field, I was pleased that this book is coming in early stage of a field that will need it more than most fields do. In most emerging research fields, a book can play a significant role in bringing some maturity to the field. Research fields advance through research papers. In research papers, however, only a limited perspective could be provided about the field, its application potential, and the techniques required and already developed in the field. A book gives such a chance. I liked the idea that there will be a book that will try to unify the field by bringing in disparate topics already available in several papers that are not easy to find and understand. I was supportive of this book project even before I had seen any material on it. The project was a brilliant and a bold idea by two active researchers. Now that I have it on my screen, it appears to be even a better idea.

Multimedia started gaining recognition in 1990s as a field. Processing, storage, communication, and capture and display technologies had advanced enough that researchers and technologists started building approaches to combine information in multiple types of signals such as audio, images, video, and text. Multimedia computing and communication techniques recognize correlated information in multiple sources as well as insufficiency of information in any individual source. By properly selecting sources to provide complementary information, such systems aspire, much like human perception system, to create a holistic picture of a situation using only partial information from separate sources.

Data mining is a direct outgrowth of progress in data storage and processing speeds. When it became possible to store large volume of data and run different statistical computations to explore all possible and even unlikely correlations among data, the field of data mining was born. Data mining allowed people to hypothesize relationships among data entities and explore support for those. This field has been put to applications in many diverse domains and keeps getting more applications. In fact many new fields are direct outgrowth of data mining and it is likely to become a powerful computational tool.

Preface

Approximately 17 million people in the USA (6% of the population) and 140 million people worldwide (this number is expected to rise to almost 300 million by the year 2025) suffer from *diabetes mellitus*. Currently, there a few dozens of commercialised devices for detecting blood glucose levels [1]. However, most of them are invasive. The development of a noninvasive method would considerably improve the quality of life for diabetic patients, facilitate their compliance for glucose monitoring, and reduce complications and mortality associated with this disease. Noninvasive and continuous monitoring of glucose concentration in blood and tissues is one of the most challenging and exciting applications of optics in medicine. The major difficulty in development and clinical application of optical noninvasive blood glucose sensors is associated with very low signal produced by glucose molecules. This results in low sensitivity and specificity of glucose monitoring by optical methods and needs a lot of efforts to overcome this difficulty.

A wide range of optical technologies have been designed in attempts to develop robust noninvasive methods for glucose sensing. The methods include infrared absorption, near-infrared scattering, Raman, fluorescent, and thermal gradient spectroscopies, as well as polarimetric, polarization heterodyning, photonic crystal, optoacoustic, optothermal, and optical coherence tomography (OCT) techniques [1-31].

For example, the polarimetric quantification of glucose is based on the phenomenon of optical rotatory dispersion, whereby a chiral molecule in an aqueous solution rotates the plane of linearly polarized light passing through the solution. The angle of rotation depends linearly on the concentration of the chiral species, the pathlength through the sample, and the molecule specific rotation. However, polarization sensitive optical technique makes it difficult to measure *in vivo* glucose concentration in blood through the skin because of the strong light scattering which causes light depolarization. For this reason, the anterior chamber of the eye has been suggested as a sight well suited for polarimetric measurements, since scattering in the eye is generally very low compared to that in other tissues, and a high correlation exists between the glucose in the blood and in the aqueous humor. The high accuracy of anterior eye chamber measurements is also due to the low concentration of optically active aqueous proteins within the aqueous humor.

On the other hand, the concept of noninvasive blood glucose sensing using the scattering properties of blood and tissues as an alternative to spectral

absorption and polarization methods for monitoring of physiological glucose concentrations in diabetic patients has been under intensive discussion for the last decade. Many of the considered effects, such as changing of the size, refractive index, packing, and aggregation of RBC under glucose variation, are important for glucose monitoring in diabetic patients. Indeed, at physiological concentrations of glucose, ranging from 40 to 400 mg/dl, the role of some of the effects may be modified, and some other effects, such as glucose penetration inside the RBC and the followed hemoglobin glycation, may be important [30-32].

Noninvasive determination of glucose was attempted using light scattering of skin tissue components measured by a spatially-resolved diffuse reflectance or NIR frequency-domain reflectance techniques. Both approaches are based on change in glucose concentration, which affects the refractive index mismatch between the interstitial fluid and tissue fibers, and hence reduces scattering coefficient. A glucose clamp experiment showed that reduced scattering coefficient measured in the visible range qualitatively tracked changes in blood glucose concentration for the volunteer with diabetes studied.

List of Figures

List of Tables

Contents

Symbol Description

α	To solve the generator maintenance scheduling, in the past, several mathematical techniques have been applied.
σ^2	These include integer programming, integer linear programming, dynamic programming, branch and bound etc.
$\sum$	Several heuristic search algorithms have also been developed. In recent years expert systems,
abc	fuzzy approaches, simulated annealing and genetic algorithms have also been tested.
$\theta\sqrt{abc}$	This paper presents a survey of the literature
ζ	over the past fifteen years in the generator
∂	maintenance scheduling. The objective is to
sdf	present a clear picture of the available recent literature
ewq	of the problem, the constraints and the other aspects of
bvcn	the generator maintenance schedule.

Part I

This is a Part

Chapter 1

Physics-based methods of failure analysis and diagnostics in human space flight

V.N. Smelyanskiy

NASA Ames Research Center, MS 269-3, Moffett Field, CA, 94035, USA

D.G. Luchinsky

Mission Critical Technologies Inc., 2041 Rosecrans Ave., Suite 225 El Segundo, CA 90245, USA

V. Hafiychuk

SGT Inc, 7701 Greenbelt Road, Suite 400, Greenbelt, Maryland 20770, USA

V.V. Osipov

Mission Critical Technologies Inc., 2041 Rosecrans Ave., Suite 225 El Segundo, CA 90245, USA

I. Kulikov

California Institute of Technology, 4800 Oak Grove Drive, Pasadena, CA 91109

A. Patterson-Hein

NASA Ames Research Center, MS 269-3, Moffett Field, CA, 94035, USA

J.Hanson

Marshal Space Flight Center/EV40, Huntsville, AL, 35812

1.1 Introduction

The Integrated Health Management (IHM) for the future aerospace systems requires to interface models of multiple subsystems in an efficient and accurate information environment at the earlier stages of system design. The complexity of modern aeronautic and aircraft systems (including e.g. the power distribution, flight control, solid and liquid motors) dictates employment of hybrid models and high-level reasoners for analysing mixed continuous and discrete information flow involving multiple modes of operation in uncertain environments, unknown state variables, heterogeneous software and hardware components.

To provide the information link between key design/performance parameters and high-level reasoners we rely on development of multi-physics performance models, distributed sensors networks, and fault diagnostic and prognostic (FD&P) technologies [38] in close collaboration with system designers. The main challenges of our research are related to the in-flight assessment of the structural stability, engine performance, and trajectory control. The main goal is to develop an intelligent IHM that not only enhances components and system reliability, but also provides a post-flight feedback helping to optimize design of the next generation of aerospace systems. Our efforts are concentrated on several directions of the research. One of the key components of our strategy is an innovative approach to the diagnostics/prognostics based on the real time dynamical inference (DI) technologies extended to encompass hybrid systems with hidden state trajectories. The major investments are into the multiphysics performance modelling that provides an access of the FD&P technologies to the main performance parameters of e.g. solid and liquid rocket motors and composite materials of the nozzle and case.

Some of the recent results of our research are discussed in this chapter. We begin by introducing the problem of dynamical inference of stochastic nonlinear models and reviewing earlier results. Next, we present our analytical approach to the solution of this problem based on the path integral formulation. The resulting algorithm does not require an extensive global search

for the model parameters, provides optimal compensation for the effects of dynamical noise, and is robust for a broad range of dynamical models. In the following Section the strengths of the algorithm are illustrated illustrated by inferring the parameters of the stochastic Lorenz system and comparing the results with those of earlier research. Next, we discuss a number of recent results in application to the development of the IHM for aerospace system.

Firstly, we apply dynamical inference approach to a solution of classical three tank problems with mixed unknown continuous and binary parameters. The problem is considered in the context of ground support system for filling fuel tanks of liquid rocket motors. It is shown that the DI algorithm is well suited for successful solution of a hybrid version of this benchmark problem even in the presence of additional periodic and stochastic perturbation of unknown strength.

Secondly, we illustrate our approach by its application to an analysis of the nozzle fault in a solid rocket motor (SRM). The internal ballistics of the SRM is modelled as a set of one-dimensional partial differential equations coupled to the dynamics of the propellant regression. In this example we are specifically focussed on the inference of discrete and continuous parameters of the nozzle blocking fault and on the possibility of an application of the DI algorithm to reducing the probability of "misses" of an on-board FD&P for SRM.

In the next section re-contact problem caused by first stage/upper stage separation failure is discussed. The reaction forces imposed on the nozzle of the upper stage during the re-contact and their connection to the nozzle damage and to the thrust vector control (TVC) signal are obtained. It is shown that transient impact induced torque can be modelled as a response of an effective damped oscillator. A possible application of the DI algorithm to the inference of damage parameters and predicting fault dynamics ahead of time using the actuator signal is discussed.

Finally, we formulate Baesian inferential framework for development of the IHM system for in-flight structural health monitoring (SHM) of composite materials. We consider the signal generated by piezoelectric actuator mounted on composite structure generating elastic waves in it. The signal received by the sensor is than compared with the baseline signal. The possibility of damage inference is discussed in the context of development of the SHM.

1.2 Dynamical inference of stochastic nonlinear models

Complex phenomena in nature and technology can often be modeled successfully by stochastic nonlinear dynamical systems, thereby facilitating the diagnosis of faults, the prognosis of future conditions, and control. Examples range from models from molecular motors [47] to epidemiology [18] and

from solid rocket motors [40] to coupled matter radiation systems in astrophysics [14].

The problem of inferring the parameters of such models from time-series data has therefore attracted much attention over the last decade. Although no general method exists for inferring the parameters of stochastic nonlinear dynamical models from measurements, various schemes have been proposed [33, 20, 22, 35, 19, 42, 48, 45]. An important numerical technique, suggested in [43, 20], is based on estimating drift and diffusion coefficients at a number of points in the phase space of the dynamical system. A particle filter approach [23] and the Markov Chain Monte-Carlo (MCMC) approach [13] were applied successfully to reconstruct the model parameters alone.

Arguably the most general approach to the solution of this problem can be obtained within Bayesian inferential framework [22, 35, 11]. The Bayesian method was used for parameter estimation in maps in the presence of dynamical [34] and weak measurement [35] noise and was applied to inference of continuous systems in [19].

A common drawback of these earlier works is their reliance on numerical methods for the optimization of cost functions. This disadvantage becomes increasingly more pronounced when inferring on-board complex aerospace systems. Another deficiency is that most of the earlier works deal with discrete maps, and the corresponding results are therefore not immediately applicable to continuous systems. This problem was addressed in [19], however, an *ad hoc* likelihood function was used there.

We now formulate the problem and present its solution using path integral approach within Bayesian inferential framework.

The time-series data of the control variables is usually observed at sequential time instants and are related to the unknown "tru" system L-dimensional states via the measurement model. In these settings the following formulation of the problem of dynamical inference is commonly adopted. Given M-dimensional time-series data $\mathcal{Y} = \{\mathbf{y}_n \equiv \mathbf{y}(t_n)\}$ $(t_n = nh)$, how can one infer the time variation of the unknown model parameters and the unknown dynamical trajectory $\mathcal{M} = \left\{\mathbf{c}(t), \mathbf{b}(t), \hat{\mathbf{D}}, \hat{\mathbf{M}}, \{\mathbf{x}_n\}\right\}$? It is assumed that the underlying dynamics can be described by a set of L-dimensional $(L \geq M)$ stochastic differential equations of form

$$\dot{\mathbf{x}}(t) = \mathbf{f}(\mathbf{x}|\mathbf{c}) + \sqrt{\hat{\mathbf{D}}}\boldsymbol{\xi}(t), \tag{1.1}$$

and the observations $\mathcal{Y}$ are related to the actual unknown dynamical variables $\mathcal{X} = \{\mathbf{x}_n \equiv \mathbf{x}(t_n)\}$ via the following measurement equation

$$\mathbf{y}(t) = \mathbf{g}(\mathbf{x}|\mathbf{b}) + \sqrt{\hat{\mathbf{M}}}\boldsymbol{\eta}(t). \tag{1.2}$$

Here $\hat{X}$ is an $M \times L$ measurement matrix, $\boldsymbol{\xi}(t)$ and $\boldsymbol{\eta}(t)$ are L- and M-dimensional Gaussian white noises, and $\hat{\mathbf{D}}$ and $\hat{\mathbf{M}}$ are $L \times L$ and $M \times M$ dimensional dynamical and measurement diffusion matrices respectively.

The solution of this problem is given by the so-called *posterior* probability density function (PDF) $\rho_{\rm post}(\mathcal{M}|\mathcal{Y})$ of the unknown parameters $\mathcal{M}$ conditioned on observations. In Bayesian model inference, the *posterior* PDF is related to the *prior* $p_{\rm pr}(\mathcal{M})$ PDF via Bayes' theorem [15]:

$$\rho_{\rm post}(\mathcal{M}|\mathcal{Y}) = \frac{\ell(\mathcal{Y}|\mathcal{M})\,\rho_{\rm prior}(\mathcal{M})}{\int \ell(\mathcal{Y}|\mathcal{M})\,\rho_{\rm prior}(\mathcal{M})d\mathcal{M}} \tag{1.3}$$

Here, the *likelihood* function $\ell(\mathcal{Y}|\mathcal{M})$ is the probability density to observe $\{\mathbf{y}_n(t)\}$ given choice $\mathcal{M}$ of the dynamical model. Meanwhile, the prior acts as a regularizer, concentrating the parameter search to those regions of the model space favored by our expertise and any available auxiliary information. This initial assignment of probabilities must be "coherent" [24], i.e., consistent with the physics of the problem. In practice, (1.3) can be applied iteratively using a sequence of data blocks $\mathcal{Y}, \mathcal{Y}', \ldots$; the posterior computed from block $\mathcal{Y}$ serves as the prior for the next block $\mathcal{Y}'$, etc. For a sufficiently large number of observations, $p_{\rm ps}(\mathcal{M}|\mathcal{Y}, \mathcal{Y}', \ldots)$ becomes sharply peaked around a most probable model $\mathcal{M}^*$.

If the sampling is dense enough the problem can be conveniently solved using Euler mid-point discretization of Eqs. (1.1), (1.2) in the form

$$\left.\begin{array}{rcl} \mathbf{x}_{n+1} &=& \mathbf{x}_n + h\,\mathbf{f}(\mathbf{x}_n^*|\mathbf{c}) + \sqrt{h}\,\hat{\mathbf{D}}\boldsymbol{\xi}_n, \\ \mathbf{y}_n &=& \mathbf{g}(\mathbf{x}_n|\mathbf{b}) + \hat{\mathbf{M}}\boldsymbol{\eta}_n, \end{array}\right\} \tag{1.4}$$

where $\mathbf{x}_n^* = (\mathbf{x}_{n+1} + \mathbf{x}_n)/2$. It was shown earlier (see e.g. [**?**, 46]) that for independent sources of white Gaussian noise in (1.4) the probability to observe $\mathbf{y}_n$ at each time step can be factorized and written in the form

$$\begin{aligned} \rho(\mathbf{y}_{n+1}|\mathbf{x}_n, \mathbf{c}) = \int \frac{\mathrm{d}\mathbf{x}_{n+1}}{\sqrt{(2\pi)^M|\hat{\mathbf{M}}|}}\, e^{-\frac{1}{2}\,[\mathbf{y}_{n+1}-\mathbf{g}(\mathbf{x}_{n+1}|\mathbf{b})]^{\rm T}\,\hat{\mathbf{M}}^{-1}\,[\mathbf{y}_{n+1}-\mathbf{g}(\mathbf{x}_{n+1}|\mathbf{b})]} \\ \times \frac{1}{\sqrt{(2\pi h)^L|\hat{\mathbf{D}}|}}\, e^{-\frac{h}{2}\,[\dot{\mathbf{x}}_n-\mathbf{f}(\mathbf{x}_n^*|\mathbf{c})]^{\rm T}\,\hat{\mathbf{D}}^{-1}\,[\dot{\mathbf{x}}_n-\mathbf{f}(\mathbf{x}_n^*|\mathbf{c})]-\frac{h}{2}\nabla.(\mathbf{f}(\mathbf{x}_n)|\mathbf{c})}. \end{aligned} \tag{1.5}$$

Summation over all the discretization points $n = 0...N-1$ yields the following result for the minus log-likelihood function $S = S_{dyn} + S_{meas} = -\ln \ell(\mathcal{Y}|\mathcal{M})$

$$\begin{aligned} S &= \frac{N}{2}\ln|\hat{\mathbf{D}}| + \frac{h}{2}\sum_{n=0}^{N-1}\Big\{\nabla.(\mathbf{f}(\mathbf{x}_n)|\mathbf{c}) + [\dot{\mathbf{x}}_n - \mathbf{f}(\mathbf{x}_n^*|\mathbf{c})]^{\rm T}\,\hat{\mathbf{D}}^{-1}\,[\dot{\mathbf{x}}_n - \mathbf{f}(\mathbf{x}_n^*|\mathbf{c})]\Big\} \\ &+ \frac{N}{2}\ln|\hat{\mathbf{M}}| + \frac{1}{2}\sum_{n=1}^{N}[\mathbf{y}_n - \mathbf{g}(\mathbf{y}_n, \mathbf{x}_n|\mathbf{b})]^{\rm T}\,\hat{\mathbf{M}}^{-1}\,[\mathbf{y}_n - \mathbf{g}(\mathbf{y}_n, \mathbf{x}_n|\mathbf{b})] \\ &+ (L+M)N\ln(2\pi h). \end{aligned} \tag{1.6}$$

where $\dot{\mathbf{x}}_n = \frac{\mathbf{x}_{n+1}-\mathbf{x}_n}{h}$. Here S_{dyn} and S_{meas} are the dynamical (first two terms) and measurement (next two terms) parts of the minus log-likelihood function. We note that S_{dyn} is the minus log-probability density in the space of dynamical paths and, in the limit of $N \to \infty$, $h \to 0$, $T = Nh = \text{const}$, it coincides with the path-integral presentation obtained earlier in [21, 17].

To find the general solution of the problem (1.1), (1.2) one can iterate optimization of S in the space of dynamical paths $\{\mathbf{x}_n\}$ and in the space of parameters $\left\{\mathbf{c}, \mathbf{b}, \hat{\mathbf{D}}, \hat{\mathbf{M}}\right\}$ (see [46]). From the view point of practical applications for on-board IVHM system it is important to avoid heavy numerical computations and to restrict the solution to an analytical one whenever it is possible. It was shown in our earlier work that analytical solution can be obtained if prior PDFs for $\mathbf{c}$, and $\mathbf{b}$ are chosen in the form of Gaussian distributions, and prior PDFs for $\hat{\mathbf{D}}$ and $\hat{\mathbf{M}}$ are uniform.

Another key ingredient of analytical approach is successful factorization of the vector field. A general form of factorization that has proved to be very effective in many interdisciplinary applications can be written as follows [45, 46, 28, 30] , including specifically aerospace applications [37, 36]

$$\mathbf{f}(\mathbf{x}|\mathbf{c}) = \hat{\mathbf{F}}(\mathbf{x})\,\mathbf{c}, \quad \mathbf{g}(\mathbf{y},\mathbf{x}|\mathbf{b}) = \hat{\mathbf{G}}(\mathbf{y},\mathbf{x})\,\mathbf{b}, \tag{1.7}$$

where $\hat{\mathbf{F}}(\mathbf{x})$ and $\hat{\mathbf{G}}(\mathbf{y},\mathbf{x})$ are $((F\times L)\times L)$ and $((G\times M)\times M)$ matrices consisting of F (G) of diagonal blocks multiplied by $\phi_i(\mathbf{x})$ $(\psi_j(\mathbf{y},\mathbf{x}))$ base functions of factorization. The F- and G-dimensional sets of base functions $\{\phi_i\}$ and $\{\psi_i\}$ are arbitrary and known.

For the chosen above prior PDFs and factorized vector fields the analytical solution can be used to infer model parameters (cf with [46, 30])

$$\langle\hat{\mathbf{D}}\rangle = \frac{h}{N}\sum_{n=0}^{N-1}\left[\dot{\mathbf{x}}_n - \hat{\mathbf{F}}_n\,\mathbf{c}\right]\left[\dot{\mathbf{x}}_n - \hat{\mathbf{F}}_n\,\mathbf{c}\right]^{\mathrm{T}}, \tag{1.8}$$

$$\langle\mathbf{c}\rangle = \hat{\mathbf{\Xi}}_{\mathcal{X}}^{-1}(\hat{\mathbf{D}})\,\mathbf{w}_{\mathcal{X}}(\hat{\mathbf{D}}), \tag{1.9}$$

$$\mathbf{w}_{\mathcal{X}}(\hat{\mathbf{D}}) = h\sum_{n=0}^{N-1}\left[\hat{\mathbf{F}}_n^{\mathrm{T}}\,\mathbf{D^{-1}}\,\dot{\mathbf{x}}_{\mathbf{n}} - \frac{\mathbf{v(x_n)}}{\mathbf{2}}\right], \tag{1.10}$$

$$\hat{\mathbf{\Xi}}_{\mathcal{X}}(\hat{\mathbf{D}}) = h\sum_{n=0}^{N-1}\hat{\mathbf{F}}_n^{\mathrm{T}}\,\hat{\mathbf{D}}^{-1}\,\hat{\mathbf{F}}_n, \tag{1.11}$$

where $\hat{\mathbf{F}}_n \equiv \hat{\mathbf{F}}(\mathbf{x}_n)$, and the components of the vector $\mathbf{v}(\mathbf{x})$ are

$$v_m(\mathbf{x}) = \sum_{l=1}^{L}\frac{\partial F_{lm}(\mathbf{x})}{\partial x_l}, \quad m = 1,\ldots,F. \tag{1.12}$$

The parameters of the measurement model can be estimated using the conditions $\frac{\partial S_{meas}}{\partial \mathbf{b}} = 0$ and $\frac{\partial S_{meas}}{\partial M_{nm}} = 0$, recovering the least square results in the

form

$$\langle \hat{\mathbf{M}} \rangle = \frac{1}{N} \sum_{n=1}^{N} \Big[\mathbf{y}_n - \hat{\mathbf{G}}_n \, \mathbf{b} \Big] \Big[\mathbf{y}_n - \hat{\mathbf{G}}_n \, \mathbf{b} \Big]^{\mathrm{T}}, \tag{1.13}$$

$$\langle \mathbf{b} \rangle = \hat{\mathbf{\Theta}}^{-1}_{\mathcal{X},\mathcal{Y}}(\hat{\mathbf{M}}) \, \mathbf{z}_{\mathcal{X},\mathcal{Y}}(\hat{\mathbf{M}}), \tag{1.14}$$

$$\mathbf{z}_{\mathcal{X},\mathcal{Y}}(\hat{\mathbf{M}}) = \sum_{n=1}^{N} \Big[\hat{\mathbf{G}}_n^{\mathrm{T}} \, \hat{\mathbf{M}}^{-1} \, \mathbf{y}_n \Big], \tag{1.15}$$

$$\hat{\mathbf{\Theta}}^{-1}_{\mathcal{X},\mathcal{Y}}(\hat{\mathbf{M}}) = h \sum_{n=0}^{N-1} \hat{\mathbf{G}}_n^{\mathrm{T}} \, \hat{\mathbf{M}}^{-1} \, \hat{\mathbf{G}}_n, \tag{1.16}$$

where $\hat{\mathbf{G}}_n \equiv \hat{\mathbf{G}}(\mathbf{y}_n, \mathbf{x}_n)$.

Eqs. (1.8)-(1.16), coupled with the optimization procedure in the paths space, represent the general Bayesian framework for learning a nonlinear stochastic dynamical system from measurements that are corrupted by noise. Using this approach we can develop a method of fast on-line tracking of the time-varying parameters of non-stationary systems, as described below.

1.3 The Lorenz system

We start with the archetypical chaotic nonlinear system of Lorenz,

$$\left.\begin{aligned} \dot{x}_1 &= \sigma \, (x_2 - x_1) + \xi_1(t), \\ \dot{x}_2 &= r \, x_1 - x_2 - x_1 \, x_3 + \xi_2(t), \\ \dot{x}_3 &= x_1 \, x_2 - b \, x_3 + \xi_3(t), \end{aligned} \right\} \tag{1.17}$$

augmented by zero-mean Gaussian noise processes $\xi_l(t)$ with covariance $\langle \xi_l(t) \, \xi_{l'}(t') \rangle = D_{ll'} \, \delta(t - t')$. Synthetic data (with no measurement noise) were generated by simulating (1.17) using the standard parameter set $\sigma = 10$, $r = 28$, $b = \frac{8}{3}$, and for various levels of dynamical noise intensities as explained below. The phase portrait of the Lorenz system with dynamical noise is shown in Figure 1.3.1 along with the noiseless case to visually convey the difficulty of the inference problem. We now demonstrate that the formalism of dynamical inference outlined in the previous section allows one both to estimate parameters of the known dynamical equations and to to effectively perform model discovery when the vector-field of the Lorenz model is assumed to be unknown. We emphasize that both algorithms work well in the presence of strong dynamical noise.

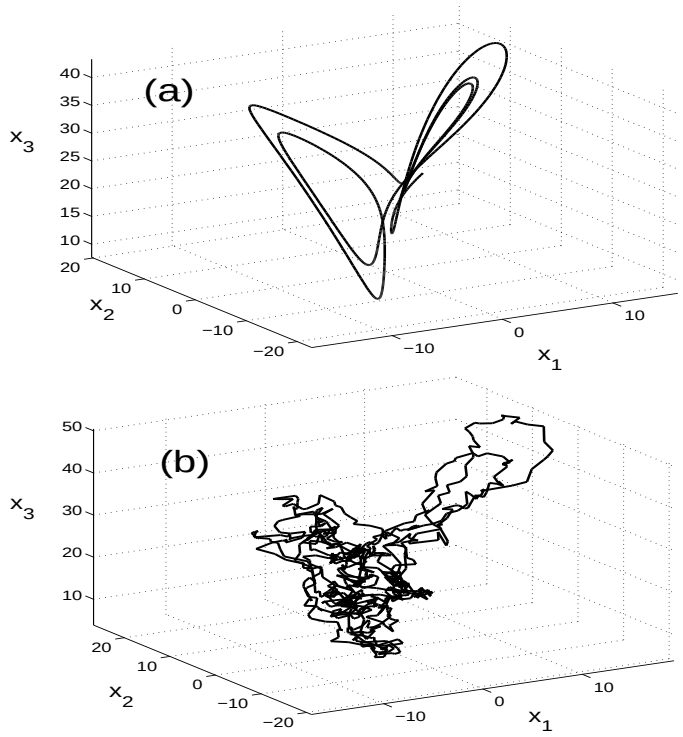

FIGURE 1.1: The phase portrait of the chaotic nonlinear Lorenz system (1.17) with the standard parameters (see text): (a) deterministic system; (b) stochastic system with strong dynamical noise, simulated with a diagonal diffusion matrix having elements $D_{11} = 1500$, $D_{22} = 1600$, and $D_{33} = 1700$. (All quantities in the equations and figures are dimensionless in this paper.)

1.3.1 Parameter estimation with strong dynamical noise

In parameter estimation, the functional form of the nonlinear force field, i.e. the right-hand side of (1.17), is assumed known, and the unknown values of the associated coefficients are then estimated from data. This is the approach reported in [19], where the diffusion matrix is taken in the form $\hat{\mathbf{D}} = \tau^2 \hat{\mathbf{I}}$, and the unknown parameters $\{\sigma, r, b, \tau^2\}$ are estimated via extensive numerical optimization of a cost function by simulated annealing and back-propagation techniques. We now demonstrate that our algorithm can estimate the parameters of the system (1.17) analytically very efficiently and with high accuracy.

First we notice that since the diffusion matrix is diagonal, our algorithm is reduces in this case to the trivial one-dimensional analytical solution of the

TABLE 1.1: Inference results for the parameters of the system (1.17) with strong dynamical noise. A synthetic data set of 4,000 points was generated for each case by simulating the system with a diffusion matrix $\hat{\mathbf{D}} = \tau^2 \hat{\mathbf{I}}$, and subsequently sampling its trajectory with $h = 0.002$.

Parameter	Value	Estimate
σ	10.00	9.9039
r	28.00	28.3004
b	2.667	2.8410
τ	40.00	39.9108

problem for each equation in the form (cf with (1.8) – (1.11)),

$$\mathbf{c}_i = \hat{\mathbf{H}}_i^{-1} \mathbf{w}_i, \qquad i = 1 \dots 3$$

where

$$w_{il} = \sum_{n=0}^{N-1} \left(c_{il}\phi_{il} - \frac{\tau^2}{2} \frac{\partial \phi_{il}}{\partial x_i} \right)$$

and

$$\hat{\mathbf{H}}_i = \sum_{n=0}^{N-1} \begin{pmatrix} \phi_{i1}\phi_{i1} & \dots & \phi_{i1}\phi_{iL} \\ \vdots & \ddots & \vdots \\ \phi_{iL}\phi_{i1} & \dots & \phi_{iL}\phi_{iL} \end{pmatrix}.$$

Noise intensity is found according to (1.8). We note that in each equation we now have different basis functions ϕ_{il}. For the first equation we have the following two basis functions: $\phi_{11} = x_1$ and $\phi_{12} = x_2$. For the second equation we have: $\phi_{21} = x_1$, $\phi_{22} = x_2$, and $\phi_{23} = x_1 x_3$. And for the last equation we have: $\phi_{31} = x_1 x_2$, $\phi_{32} = x_3$.

Thus there are a total of 8 unknown parameters to be estimated: a seven-dimensional coefficient vector $\mathbf{c}$ and the noise intensity τ^2. (Note that this is already more ambitious than what was done in [19], since we are attempting to estimate *all* model coefficients, including those that are equal to ± 1.)

The convergence of our scheme is so rapid that it is feasible to use the algorithm in real time on "streaming" data. To make a fair comparison we use the same number of data points as in [19]. As an indication of the inference accuracy, we quote in Table 1.1 results for data simulated with the standard Lorenz parameter set and two values of dynamical noise intensity for weak and strong cases.

1.3.2 Model reconstruction with strong dynamical noise

We now assume that the analytical form of the nonlinear force field of the system that generated trajectory shown in Figure 1.3.1(b) is not known

TABLE 1.2: Inference results for a representative set of parameters of the model (1.18), obtained using 200 blocks of 600,000 data points each, sampled at $h = 0.005$. True and inferred parameter values are shown along with the corresponding error (relative and absolute errors for the nonzero and zero parameters, respectively). The inference error is below 1% for all parameters, and much less for most.

Parameter	Value	Estimate	Error
a_{11}	-10.0000	-9.9984	0.0161
a_{21}	28.0000	28.0139	0.0496
a_{31}	0.0	-0.0052	-0.5180
a_{21}	10.0000	9.9982	0.0178
a_{22}	-1.0000	-1.0051	0.5120
a_{23}	0.0	0.0031	0.3072
a_{33}	-2.6667	-2.6661	0.0196
b_{111}	0.0	0.0002	0.0179
b_{211}	0.0	0.0002	0.0238
b_{311}	0.0	-0.0004	-0.0401
b_{113}	0.0	-0.0001	-0.0111
b_{213}	-1.0000	-1.0004	0.0446
D_{11}	0.2867	0.2865	0.0587
$D_{13} = D_{31}$	0.1069	0.1061	0.7657

a priori. In this setting, it is more appropriate to refer to the inference problem as model reconstruction. In practical terms, the main difference between parameter estimation and model reconstruction is in the number of unknown parameters involved, which is typically an order of magnitude larger in the latter case. To solve this problem within the formalism of dynamical inference one may adopt a parametric model of the form

$$\dot{x}_l = \sum_{l'=1}^{3} a_{ll'}\, x_{l'}(t) + \sum_{l',l''=1}^{3} b_{ll'l''}\, x_{l'}(t)\, x_{l''}(t) + \xi_l(t), \tag{1.18}$$

$l, l', l'' = 1, 2, 3$. Including the elements of the (symmetric) diffusion matrix $\hat{\mathbf{D}}$, we now have a total of 33 unknown parameters comprising the set $\mathcal{M} = \{\{a_{ll'}\}, \{b_{ll'l''}\}, \{D_{ll'}\}\}$. Despite the restriction to linear, bilinear, and quadratic polynomial basis functions, (1.18) still represents an extremely broad class of dynamical models. Assuming no measurement noise for simplicity, the application of our algorithm entails the use of equations (1.9) – (1.11).

The accuracy of the reconstruction depends on a number of factors. We have observed that it is generally possible to achieve arbitrarily accurate inference results with a (sufficiently small) fixed sampling interval by increasing the total duration of observation; this is true even in the case of a full (i.e., non-diagonal) diffusion matrix. Indeed, we were able to achieve highly accu-

rate parameter estimates for sampling intervals ranging from 10^{-6} to 0.01 and noise intensities ranging from 0 to 10^2. As an example, we summarize in Table 1.2 our inference results for the model (1.18) with a full diffusion matrix, showing extremely high accuracy.

Finally, we would like to demonstrate the importance of the Jacobian prefactor included in our likelihood function by examining the inference results obtained with and without this term. Our analysis shows that the omission of the prefactor in the likelihood function results in a systematic underestimation of this parameter, whereas the inclusion of this term leads to an accurate inference as it optimally compensates for the effects of dynamical noise.

The computational efficiency of our algorithm also allows us to lift the practical limitation on the total number of data points used for inference in previous work and to extend substantially the dimensionality of the model space. As a consequence it can be efficiently applied to deal with a more general problem of model reconstruction, when the functional form of a nonlinear vector field is unknown

We now consider a selected set of examples of dynamical inference in aerospace applications.

1.4 Three tank problem

In section we describe an application of the dynamical system algorithm to a three tank [49, 27] which is formed by a sequence of three interconnected tanks and has been declared as a benchmark for fault detection and diagnosis in dynamical system [50]. The system schematic is shown in Figure 1.4. We consider this system in the context of ground support system for liquid fuel filling system. The key feature of the analysis presented below is that the underlying dynamics is hybrid system, i.e. the system exhibits both continuous flow and discrete jumps. Accordingly a of hybrid probabilistic approach is required for its inference. It is shown that the method of dynamical inference introduced above can accommodate abrupt changes in the model parameters and can be used to develop hybrid probabilistic algorithm.

Accordingly the model equations are slightly modified to have the form

$$\begin{aligned}
\dot{h_1} &= \varepsilon_1 \sin(\omega t) - c_{12}\left(\xi\left[h_1 - H_{12}\right] - \xi\left[h_2 - H_{12}\right]\right) \\
&- L_{12}\sqrt{f_0\left[h_1 - H_{12}\right]} - c_{13}\left(\xi\left[h_1 - H_{13}\right] - \xi\left[h_3 - H_{13}\right]\right) \\
&\quad -L_{13}\sqrt{f_0\left[h_1 - H_{13}\right]} + f_1\left[h_1\right] + \sigma_{11}\xi_1(t), \qquad (1.19)\\
\dot{h_2} &= -\varepsilon_2 \sin(\omega t) + c_{12}\left(\xi\left[h_1 - H_{12}\right] - \xi\left[h_2 - H_{12}\right]\right) \\
&+ c_{23}\left(\xi\left[h_3 - H_{23}\right] - \xi\left[h_2 - H_{23}\right]\right) - L_{23}\sqrt{f_0\left[h_2 - H_{23}\right]} + \sigma_{22}\xi_1(t), \\
\dot{h_3} &= \varepsilon_3 \sin(\omega t) + c_{23}\left(\xi\left[h_3 - H_{23}\right] - \xi\left[h_2 - H_{23}\right]\right) + \sigma_{33}\xi_1(t),
\end{aligned}$$

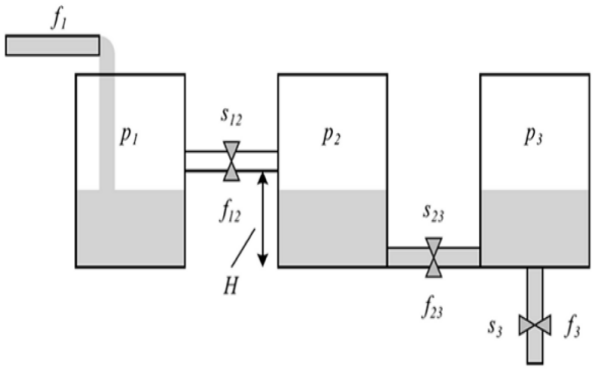

FIGURE 1.2: Schematic of Three-Tank bench Mark System.

where

$$\begin{aligned} \xi(t) &= t \cdot \theta(t); \quad f_0(t) = (1 + \tanh(a \cdot t))/2; \\ f_1(t) &= 0.2 \cdot f_0(0.2 - t) + (f_0(0.8 - x) - f_0(0.2 - t)) + \\ &\quad 0.2 \cdot (f_0(1 - t) - f_0(0.8 - t)) \end{aligned} \tag{1.20}$$

and $\theta(t)$ is the unit step function. Here H_{ij} represent liquid levels in each tank with respect to the connecting pipes, $f_1(t)$ is the known input flow, c_{ij} represent parameters of coupling between the tanks, terms proportional to ε_i correspond to the vibrations of the tanks (in the present version only tank 1 is vibrating), terms proportional to L_{ij} correspond to the leaks, finally terms proportional to σ_{ij} correspond to the random vibrations of the tanks. Here $\xi_i(t)$ are white Gaussian noises and σ_{ij} are the amplitudes of random vibrations.

The known input flow and the $f_1(t)$ and measured signals $h_1(t)$, $h_2(t)$, and $h_3(t)$ are shown in Figure 1.4. The values of the known relative heights in these simulations were $H_{12} = 0.5$, $H_{23} = 0.2$, $H_{13} = 0.6$. We emphasize that the time instants of the jumps in the flow signals $h_2(t)$ and $h_3(t)$ is not know and have to be inferred alone with other model parameters. The coefficients corresponding to the jumps are discrete parameters of our hybrid model. Note also that all three measured flow signals are perturbed by the periodic vibrations with known frequencies, but unknown amplitudes, and by random force. To apply algorithm introduced in **??** we have to specify the set of unknown variables

$$c = \{\varepsilon_1, \varepsilon_2, \varepsilon_3, c_{12}, c_{13}, c_{23}, L_{12}, L_{13}, L_{23}, D_{11}, D_{22}, D_{33}\}\,. \tag{1.21}$$

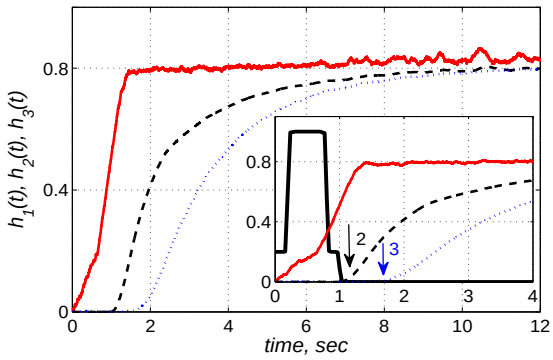

FIGURE 1.3: Measured flow signals for the three tank benchmark system are shown by red solid line for $h_1(t)$, black dashed line for $h_2(t)$, and by red dotted line for $h_3(t)$. The measured signals are compared with the input flow (black thick line) in the inset. The location of jumps for flows $h_2(t)$ and $h_3(t)$ are indicated by the arrows.

and F-dimensional (F=9) set of the base functions

$$\begin{aligned}\{\phi_i(x,t)\} = \Big\{ &\sin(\omega t), \left(\xi\left[h_1 - H_{12}\right] - \xi\left[h_2 - H_{12}\right]\right), \sqrt{\xi\left[h_1 - H_{12}\right]}, \\ &\left(\xi\left[h_1 - H_{13}\right] - \xi\left[h_3 - H_{13}\right]\right), \sqrt{\xi\left[h_1 - H_{13}\right]}, \\ &\left(\xi\left[h_1 - H_{12}\right] - \xi\left[h_2 - H_{12}\right]\right), \left(\xi\left[h_3 - H_{23}\right] - \xi\left[h_2 - H_{23}\right]\right), \\ &\sqrt{\xi\left[h_2 - H_{23}\right]}, \left(\xi\left[h_3 - H_{23}\right] - \xi\left[h_2 - H_{23}\right]\right) \Big\}.\end{aligned} \tag{1.22}$$

It is assumed for simplicity that the measurement noise is small, which is justifiedin the case of application to the ground fuel filling system. Under these assumptions the inference of the unknown parameters of the model (1.19) from the measured time-series of the flow variables is a matter of straightforward extension of equations (1.8) – (1.11). In particular one has to check on each step of iterations if the base functions corresponding to the discrete parameters are identically zero and exclude related columns and rows from matrix $\hat{\mathbf{\Xi}}_{\mathcal{X}}(\hat{\mathbf{D}})$ to avoid singularities in Eq. (1.9)

An example of convergence of one of the model parameters is shown in Figure 1.4 (b). The circles show dynamics of the mean inferred value of the parameter c_{12}. The bars show the dynamics of the corresponding standard deviation. The horizontal red line indicates the actual value of the model parameter. It can be seen from the figure that the inferred value of c_{12} approaches its true value as the total time of inference is increasing, simultaneously its standard deviation is decreasing indicating the convergence of the algorithm. Note also that initial value of coupling between tank 1 and 2 is inferred as zero. This value of the coupling parameter c_{12} corresponds to the fact that

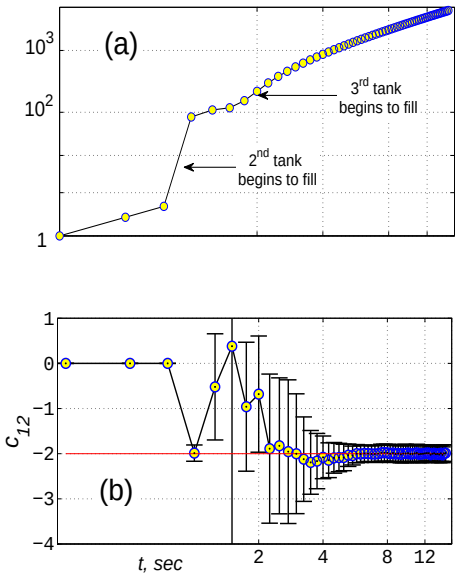

FIGURE 1.4: (a) Number of operations as function of the total time interval of inference. (b)Convergence of the dynamical inference for the c_{12} parameter. Time is shown in logarithmic scale. The horizontal red line shows the true value of the parameter c_{12}.

at the initial time the second tank is closed and there is no flow between the two tanks. Next we can see that a jump to the correct value of $c_{12} = 2$ occurs when the second tank begins to fill. Additional jump occurs when the third tank is also open (at around 2 sec). At this moment we can also observe a step-wise increase of the standard deviation indicating that the dimensionality of the system was increased in a step-wise manner. The number of operations required for convergence as a function of time is shown in Figure 1.4 (a) and is summarized in the Table 1.3.

It can be seen from the table that discrete jumps in the coupling cij and leak Lij parameters are also detected and their continuous values are inferred. However, the convergence of the parameters is highly non-uniform.

To clarify this issue let us make a few remarks. It was mentioned earlier that each block of data can be measured independently and used at the next step of inference provided that the results at previous steps are taken into account in the form of a prior distribution. In this case Eqs. (1.10)-(1.11) can be then written in the form (see [46])

$$\mathbf{w}_k = \hat{\mathbf{\Xi}}_{k-1}^{-1}\mathbf{c}_{k-1} + h\sum_{n\in N_k}\left[\hat{\mathbf{F}}_n^{\mathrm{T}}\hat{\mathbf{D}}^{-1}\dot{\mathbf{x}}_n - \frac{\mathbf{v}_n}{2}\right], \tag{1.23}$$

$$\hat{\mathbf{\Xi}}_k = \hat{\mathbf{\Xi}}_{k-1} + h\sum_{n\in N_k}\hat{\mathbf{F}}_n^{\mathrm{T}}\hat{\mathbf{D}}^{-1}\hat{\mathbf{F}}_n. \tag{1.24}$$

Applying this equations recursively one can show that the covariance matrix $\hat{\mathbf{\Xi}}_k$ of the *posterior* distribution is a sum over all the blocks and has the structure of a Kronecker product

$$\hat{\mathbf{\Xi}}_k = h\hat{\mathbf{\Phi}}\otimes\hat{\mathbf{D}}^{-1}, \tag{1.25}$$

TABLE 1.3: Inference results for a set of parameters of the model (1.19), obtained using 300 blocks of 6000 data points each, sampled at $h = 0.002$. True and inferred parameter values are shown along with the corresponding standard deviation (STD).

Parameter	**Value**	**Estimate**	**STD**
ε_1	0.1	0.0993	0.01
c_{12}	2.0	1.988	0.18
c_{13}	2.0	1.999	0.01
L_{12}	0.07	0.047	0.19
L_{13}	0.04	0.068	0.23
L_{23}	0.08	0.08	0.001
c_{23}	1.0	1.004	0.006
D_{11}	9.0×10^{-4}	8.9×10^{-4}	1.4^{-5}
D_{22}	4.0×10^{-6}	4.0×10^{-6}	1.3×10^{-7}

where

$$\hat{\mathbf{\Phi}} = \sum_{n \in N_1, \ldots, N_k} \begin{pmatrix} \psi_{1,n}\psi_{1,n} & \cdots & \psi_{1,n}\psi_{B,n} \\ \vdots & \ddots & \vdots \\ \psi_{B,n}\psi_{1,n} & \cdots & \psi_{B,n}\psi_{B,n} \end{pmatrix}, \qquad \psi_{i,n} \equiv \psi_i(x_n)$$

Accordingly, all non-zero elements of this matrix grow in time as $T = hN$. On the other hand the second term in (1.24) remains finite for a fixed number of points in one block N_k. Therefore, $\hat{\mathbf{\Xi}}_{k-1}$ approaches $\hat{\mathbf{\Xi}}_k$ for large T and c_k becomes

$$c_k \approx c_{k-1} + \hat{\mathbf{D}} \otimes \hat{\mathbf{\Phi}}_k^{-1} \sum_{n \in N_k} \left[\hat{\mathbf{F}}_n^{\mathrm{T}} \hat{\mathbf{D}}^{-1} \dot{\mathbf{x}}_n - \frac{\mathbf{v}_n}{2} \right]. \tag{1.26}$$

To analyse the leading order contribution to the residuals of $\{c_k\}$ given by the second term in (1.26) we can assume that noise matrix is known and constant, the contribution from the sum can always be finite and small for small and finite N_k. The only factor that represent the accumulating effect of convergence is $\hat{\mathbf{\Phi}}_k^{-1}$. It is clear now that convergence of the residuals is inversely proportional to the sum of eigenvalues of $\hat{\mathbf{\Phi}}_k$. Therefore the presence of large eigenvalues of $\hat{\mathbf{\Phi}}_k^{-1}$ slows down the convergence of all coefficients $\{c_k\}$.

It is also clear that the choice of the base functions has a strong effect on convergence the dynamics of the system. In particular, for polynomial base functions and small noise intensities the smallest elements of $\hat{\mathbf{\Phi}}$ correspond to the highest powers of polynomials and usually correspond to large eigenvalues of $\hat{\mathbf{\Phi}}_k^{-1}$.

Therefore, to achieve the best results in dynamical inference on-board it is important to identify the key non-stationary parameters for each fault mode and too learn most of the stationary parameters in a preliminary analysis of the system. Next, by incorporating real-time inference into the inferential

learning framework and excluding all but the most important non-stationary parameters from the tracking procedure one can improve the time resolution of the method by orders of magnitude.

We next consider an application of the dynamical inference in the context of developing on-board FD&P system for solid rocket motors.

1.5 In-flight decision support for SRMs

Safe exploration of the space require development of the new algorithms with the overarching goal of extracting an information from available data with no "misses" and no "false alarms". The existing algorithms rely heavily on the linearisation of the equations of motion and setting conservative margins for the nominal values of the control parameters. Yet a result the prognostic reliability of such algorithms is limited because of limited number of sensors available on-board, limited thrust vector control authority, and short time window between the detectable onset of a catastrophic failure. It is very desirable to embed standard algorithms into a Bayesian framework to facilitate FD&P system.

Here we demonstrate an application of the dynamical inference algorithm to a few fault scenarios including: (i) step-wise nozzle blocking with progressive steady burn-out, (ii) nozzle blocking with time varying fault parameter and neutral thrust curve modelling a possible "miss" situation, where sudden increase of the pressure follows a prolonged period of small deviations of the pressure from the nominal value; (iii) and finally we will model a possible "false alarm situation where pressure following a sudden increase in the chamber pressure, induced by a cloud of solid particles, returns to its nominal value. To simplify the discussion we restrict our analysis to the case of a subscale motor. An extension of this approach to a large segmented motors can be found in [31].

1.5.1 Internal ballistics of SRMs

The internal ballistics of the SRMs in the presence of the fault can be described by the following set of stochastic partial differential equations representing conservation laws for mass momentum, and energy of the gas (see e.g. [3, 39, 40, 31])

$$\begin{cases} \partial_t \left(A\rho\right) = -\partial_x \left(A\rho u\right) + \rho_p r_b l + d_1 \xi_1(t), \\ \partial_t \left(A\rho u\right) = -\partial_x \left(A\rho u^2\right) - A\partial_x p + \rho_p r_b l u_S + d_2 \xi_3(t), \\ \partial_t \left(A\rho e_t\right) = -\partial_x \left(A\rho h_t u\right) + H\rho_p r_b l + d_3 \xi_2(t). \end{cases} \tag{1.27}$$

Here A is the port area, $e_t = c_V T + u^2/2$ and $h_t = c_P T + u^2/2$ are the

total energy and total enthalpy of the gas flowing with velocity u, temperature T, pressure p, and density ρ. The propellant properties are described by the heat of combustion H, density ρ_p and the burning rate given by the following expression $r_b = r_c(p/p_c)^n$. To model performance of the functionally graded propellants we introduce the port perimeter $l(t,x)$ as a given by design function of the burned distance $R(x)$, e.g. for a progressive burning $l = 2\pi R$ and for a neutral thrust curve $l = const$. The burning surface is given by the integral $A_b(t) = \int_0^L l(t,x)dx$ and, therefore, is determined by the propellant grading function. The increase of the volume of the combustion chamber during the time interval h is $\Delta V = A_b(t)\Delta R$, where ΔR is given by the burning rate

$$\frac{dR}{dt} = r_b\left(p_0\right)p^n + d_4\xi_3(t). \tag{1.28}$$

To model various uncontrollable sources of noise (such as cracks and case vibrations) that may become essential in off-nominal conditions a random component in the propellant density is introduced that results in the random forcing in Eqs. (1.27) and (1.28) with amplitudes d_i. Various fault modes in SRMs can now be modelled within the set of Eqs. (1.27) by choosing the time scale and direction of the geometrical alternations of the grain and case. For example, the bore choking fault can be modelled by introducing fault induced changes to the local port area $A(x)$; the crack dynamics can be modelled by introducing crack induced changes to an effective port perimeter; the nozzle blocking and the case breach faults can be introduced as changes to the nozzle throat area A_t (see e.g. [32] and discussion below).

1.5.2 Low-dimensional performance model

To be able employ dynamical inference algorithm on-board one has to reduce model (1.27) to a set of ordinary differential equations allowing for an analytical estimation of the model parameters and their fault induced deviations. To this end we introduce a low-dimensional performance model of SRM in the "filling volume" approximation [39, 40]. For a subscale motor the ratio of the gas velocity to the stagnation speed of sound c_0 is small ($u^2/c_0^2 \ll 1$) everywhere along the propellant grain. Under these conditions one can integrate Eqs. (1.27) along the grain axis to obtain

$$\begin{cases} \partial_t\left(\rho_0 V\right) = -\left(\rho u A\right)\big|_L + \rho_p r_b(p_0)A_b + \tilde{d}_1\xi_1(t), \\ \partial_t\left(\rho_0 e_0 V\right) = -\left(\rho u A h_t\right)\big|_L + H\rho_p r_b(p_0)A_b + \tilde{d}_2\xi_2(t), \\ \partial_t R = r_b\left(p_0\right), \end{cases} \tag{1.29}$$

where subindex 0 corresponds to stagnation values of the flow parameters. Finally, taking into account the sonic condition at the nozzle throat in the form

$$\left(A\rho u\right)\big|_L = \rho_t u_t A_t, \tag{1.30}$$

and introducing dimensionless variables (normalized by arbitrary reference values of pressure and density p_s and ρ_s)

$$p \to p_0/p_s; \quad \rho \to \rho_0/\rho_s \tag{1.31}$$

we arrive at the following from of the low-dimensional performance model (LDPM) of the SRM operation in nominal and off-nominal regimes

$$\begin{aligned}
\frac{dp}{dt} &= -\frac{c_0\gamma\Gamma A_t(t)}{V(t)}p\sqrt{p/\rho} + \frac{A_b(t)r_b}{V(t)}\left(\gamma\rho_p - p\right)p^n + \frac{\tilde{d}_2\left(\gamma-1\right)}{V(t)}\xi_2(t), \\
\frac{d\rho}{dt} &= -\frac{c_0\Gamma A_t(t)}{V(t)}\sqrt{p\rho} + \frac{A_b(t)r_b}{V(t)}\left(\rho_p - \rho\right)p^n + \frac{\tilde{d}_1}{V(t)}\xi_1(t), \\
\frac{dR}{dt} &= r_b p^n + \tilde{d}_3\xi_3(t), \quad \dot{V} = A_b(t)r_b p^n.
\end{aligned} \tag{1.32}$$

Here the burning area $A_b(t) = f(R(t))$ is given by the design of the propellant grading and is a function of R. It is now possible to characterize the dynamics of the SMB operation by the parameters averaged over the length of the combustion camera. For example, the cracking and bore chocking faults will affect $A_b(t)$ and $V(t)$, while the nozzle failure or the case breach faults may affect $A_t(t)$, the growing intensity of the noise can also be an important indication of the fault. The dynamics of the fault in these settings is characterized by an unknown time-dependent fault function $f_{fault}(t)$ that in many cases of interest can be assumed to be a polynomial function of time with unknown coefficients. We now demonstrate that abrupt changes of the model parameters can be accommodated within introduced Bayesian inferential framework of on-board FD&P system for SRMs.

1.5.3 Estimation of the parameters of nozzle blocking

In our first example we consider inference of the nozzle blocking fault modelled as a step-wise change in the nozzle throat area A_t. An additional rationale behind this example is that the significant step-wise change in the parameters of nonlinear models is one of the most plausible reasons for the failure of alternative Kalman-filter based algorithms. The nozzle blocking is modelled as a sudden change of the nozzle area to the effective value $A_{et} = A_t + \Delta A_t$ (cf. [32]). The corresponding geometry change of the nozzle is shown in Figure 1.5.3(a). To estimate the change of the nozzle area we notice that it is the coefficient $a = \frac{c_0\gamma\Gamma A_t(t)}{V(t)}$, which is proportional to A_t. We also notice that time-series $R(t)$, $V(t)$, and $A_b(t)$ are completely determined by the time-trace of pressure $p(t)$ and can be excluded from the inference algorithm. The results of dynamical inference obtained using this algorithm are shown in Figure 1.5.3(b) and summarized in the Table 1.4

It can be seen that the dynamical inference algorithm provides an accurate estimation of abruptly changing SRM parameters and that parameter' PDFs become sharply peaked about the true value.

TABLE 1.4: The results of the parameter estimation of the model (1.27). The total time of the measurements in this test was t=0.5 sec, the sampling time was h=0.001 sec, and the number of measured points was N=500. The propellant grain has cylindrical geometry.

Parameter	Value	Estimate	Relative Error
$2\gamma\rho_p$	2575.34	2572	1.1%
$-(c_0\gamma\Gamma A_t)/V$	-1101.75	-1103	1.1%
d_1^2	0.0902	0.0906	0.4%
d_2^2	0.0902	0.0906	0.4%

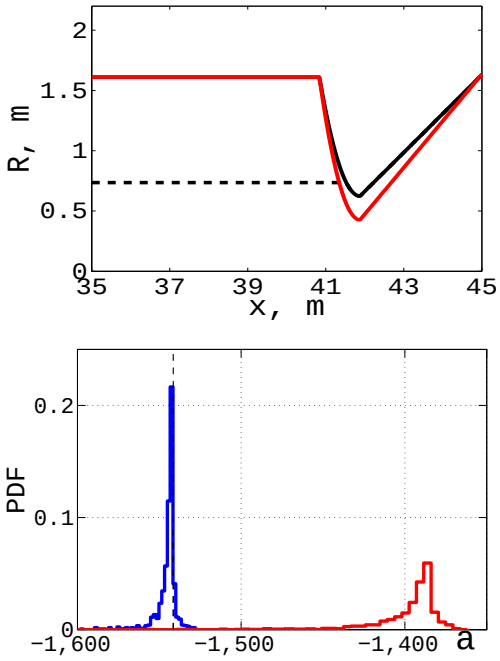

FIGURE 1.5: (a) Geometry of the nozzle blocking model. The contour of the combustion chamber before the fault is shown by the black solid line and after the fault by the red line. The grain location is shown by the dashed line. (b) Estimation of the value of the parameter a before (left curve) and after (right curve) the fault. The dashed line shows the actual value of the parameter. The solid lines show the PDF of the parameter estimation with t=0.5 sec, h=0.001 sec, N=500.

1.5.4 Predicting "misses" in the fault detection

To illustrate prediction of "misses" in on-board FD&P system let us consider a situation when small pressure induced deviation from the nominal

value persists for a few second prior to the rapid crossing the "alarm" level. Such fault dynamics is typical for combustion instabilities in solid propellant motors [12] and represents an archetypal example of "misses".

This situation is illustrated in Figure 1.5.4, where measured pressure signal (black solid line) crosses the alarm level (dashed line) and this initiating the alarm at approximately $t_A = 15$ sec. The overpressure fault occurs at $t_F = 17$ sec and the time window between the alarm and a "catastrophic" event becomes too short, which can be considered as a model of "miss" situation. We model the "misses" by introducing fault-induced changes to the nozzle throat area and assume that the time evolution of the nozzle fault is highly nonlinear and can be described by a polynomial function

$$A_{et} = A_{t0} - \left(\alpha\tau + \beta\tau^2 + \delta\tau^3\right). \tag{1.33}$$

This polynomial approximation of the fault dynamics is substituted into Eqs. (1.32). It is the presence of high-powers of time the cause rapid deviation of pressure from the nominal value at $t_F = 17$ sec. The earlier detection of "misses" in this context is reduced to a two-step procedure: (i) detection of the fault initiation and (ii) earlier detection of high-power terms in the polynomial fit to the time evolution of the fault. Accordingly, the pressure time-traces have to be followed continuously on-line and fast algorithm of dynamical inference has to be employed for on-board estimation of the fault parameters.

To simplify further discussion we neglect random term in the equation for the burn distance and assume that the thrust curve is neutral. Then burn distance, burning area, and the combustion chamber volume are a known

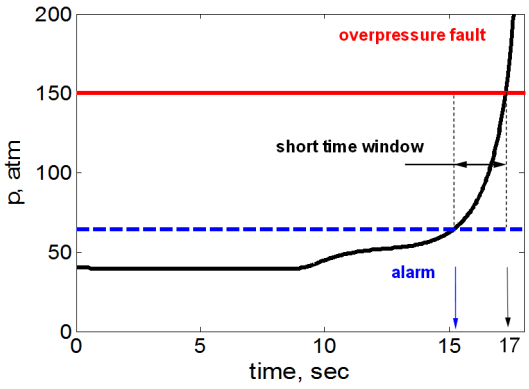

FIGURE 1.6: Example of possible time variation of the pressure fault (black line) representing a possible "miss" situation. The blue dashed and red solid lines indicate the "alarm" and the "catastrophe" levels respectively. Note that the time window between the "alarm" and the "catastrophe" is too short.

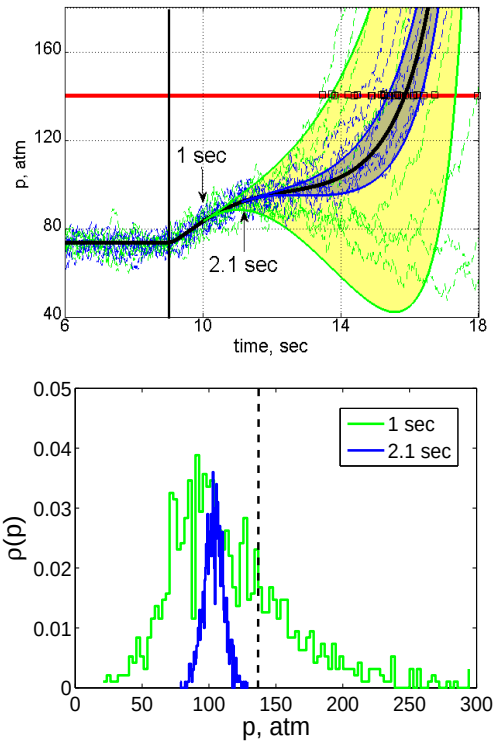

FIGURE 1.7: (top) Time evolution of the pressure build up after the nozzle blocking fault is shown by the back solid line. The results of the predictions build 1 sec and 2.1 sec after the fault are shown by green and blue lines correspondingly. Examples of the pressure time-traces predicted ahead of time using inferred values of the fault parameters are shown by the jiggling lines. The green lines bounding yellow shaded area indicate standard deviations of the predictions after 1 sec of inference. The blue lines bounding blue shaded area indicate standard deviations of the predictions after 2.1 sec of inference. The time moments of the predicted overpressure faults used to build the PDF of the case burst times as shown by the black circles on the red margin line. Fault occurs at $t = 9$ sec. (bottom) The PDF of the predicted values of pressure at t=14 sec build 1 sec (green line) and 2.1 sec (blue lines) after the fault. The dashed vertical line shows the dangerous level of the pressure.

functions of the pressure time-trace

$$R(t) = r_b \int_0^t p^n(t')dt'; \quad A_b(t) = A_{b0} = const; \quad V(t) = V_0 + A_{b0}R(t) \quad (1.34)$$

and the equations of the SRM internal ballistics take the form

$$\begin{aligned} \frac{dp}{dt} &= -\frac{c_0\gamma\Gamma A_{et}(t)}{r_b V(t)} p\sqrt{p/\rho} + \frac{p^n}{R(t)}\left(\gamma\rho_p - p\right) + d_2'\xi_2(t), \qquad (1.35) \\ \frac{d\rho}{dt} &= -\frac{c_0\Gamma A_{et}}{r_b V(t)}\sqrt{p\rho} + \frac{p^n}{R(t)}\left(\rho_p - \rho\right) + d_1'\xi_1(t), \end{aligned}$$

where we have introduced dimensionless time $t \to r_b t$, appropriately scaled constant unknown noise intensities d_1' and d_2', effective throat area $A_{et}(t)$ given by Eq. (1.33), and $R'(t) = V_0/A_{b0} + R(t)$.

To apply an algorithm of dynamical inference we rewrite the factorized vector field in the form $f(x,t) = \hat{C}\phi$. The set of the base function can be chosen in the form

$$\{\phi_i(t)\} = \left\{ \tfrac{p^n}{R'}, \tfrac{p^{n+1}}{R'}, \tfrac{p^n\rho}{R'}, \sqrt{\tfrac{p}{\rho}}\tfrac{p}{R'}, \sqrt{\tfrac{p}{\rho}}\tfrac{p\tau}{R'}, \dots \right.$$
$$\left. \sqrt{\tfrac{p}{\rho}}\tfrac{p\tau^2}{R'}, \sqrt{\tfrac{p}{\rho}}\tfrac{p\tau^3}{R'}, \sqrt{\tfrac{p}{\rho}}\tfrac{\rho}{R'}, \sqrt{p\rho}\tfrac{\tau}{R'}, \sqrt{p\rho}\tfrac{\tau^2}{R'}, \sqrt{p\rho}\tfrac{\tau^3}{R'} \right\}.$$

And the matrix $\hat{C}$ can be written as follows

$$\hat{C} = \begin{bmatrix} \gamma\rho_p & -1 & 0 & -a\gamma & -a\gamma\alpha' & -a\gamma\beta' & -a\gamma\delta' & 0 & 0 & 0 & 0 \\ \rho_p & 0 & -1 & 0 & 0 & 0 & 0 & -a & -a\alpha' & -a\beta' & -a\delta' \end{bmatrix}.$$

Here $a = (c_0\Gamma A_{t0})/(r_b V_0)$ and coefficients α', β', and δ' are equal to the coefficients α, β, and δ in Eq. (1.33) scaled by A_{b0}/V_0.

The results of the detecting the "misses" are shown in Figure 1.5.4. To detect fault initiation parameters of the system are monitored in real time. Once fault is detected at time t_d the algorithm is continuously updating the inferred values of parameters estimated on increasing intervals of time elapsed from t_d. These values are used to generate a set of trajectories predicting pressure dynamics and to calculate PDFs of pressure ahead of time and of the instants of time corresponding to the case burst. Example of trajectories generated for two different time intervals 1 sec and 2.1 sec are shown in Figure 1.5.4 (a) by green and blue lines respectively. Examples of the PDFs of the time moment of the overpressure fault are shown in Figure 1.5.4 (b). It can be seen from the figure that predicted PDFs converges to the correct value 2.1 sec after the fault extending the time window between the "alarm" and the fault almost three folds (cf. with Figure 1.5.4) and reducing the probability of the "misses". Further detailed discussion and examples of application to an analysis of the results of the ground firing test and to a case breach fault diagnostic and prognostic in a large segmented SRM are give [29].

1.6 Diagnostics of space vehicle stage separation failure

The stage separation failure may have various origins including e.g. failure of the accelerating/decelerating motors during the separation. The combined expected failure rate is relatively high and is the second most common cause of launch failures [6]. Despite this fact a reliable in-flight diagnostic and prognostic system for stage separation failure is currently unavailable. Below we report a progress in development of such system. Development of an in-flight FD&P system for the stage separation failure is a challenging engineering problem [41]. The main difficulties stem from the fact that the phenomena underlying fault dynamics are highly non-linear and transient in structural, thermal, and fluid dynamical domains. Accordingly, the solution requires 3D analysis of the thermal/fluid/structure interaction in the supersonic flow. In addition the number of sensors available on-board is severely limited and the safe time window between the detectable onset of the fault and possible catastrophic failure is typically a few seconds. To overcome these difficulties we use a combination of the physics based analytical model and high-fidelity simulations using ABAQUS [1] and FLUENT [2].

We investigate a problem of the second stage engine nozzle damage due to the impact with the first stage of the vehicle in the process of stage separation. We describe high-fidelity method for analytical estimations of structural dynamics of the second stage engine nozzle, analyze nozzle damage due to the re-contact of the stages and discuss the results of the computer simulations of re-contact process. We describe method of nozzle damage diagnostics in real time using vehicle sensor data.

1.6.1 Nozzle extension impact dynamics

We consider two-stage, vertically stacked space vehicle. The vehicle is propelled by the first stage booster at the first phase of the flight. After the rocket booster completes its mission, the stages separate and the second stage engine provides the propulsion during the second phase of the flight. Due to separation faults, the first stage can collide with the second stage engine nozzle and damage it. As the first task we perform the analytical description of nozzle damage after the impact using finite element model and the theory of shells. Dynamics of the second stage engine nozzle extension under the impact is well approximated by Donnell's shallow shell theory. Dynamics of the second stage engine nozzle extension under the impact is well approximated by Donnell's equation of shallow shell theory [26]

$$D\Delta^2 w - \nabla_R^2 F + ch\frac{\partial w}{\partial t} + \rho h\frac{\partial^2 w}{\partial t^2} = f(t, s, \theta), \tag{1.36}$$

$$\frac{1}{G}\Delta^2 F + \nabla_R^2 w = 0, \tag{1.37}$$

where w transverse displacement, F - an Airy type of stress function

$$\Delta = \frac{\partial^2}{\partial s^2} + \frac{1}{s}\frac{\partial}{\partial s} + \frac{1}{s^2 \sin^2\alpha}\frac{\partial^2}{\partial \theta^2}, \nabla_R^2 = \frac{1}{s\tan\alpha}\frac{\partial^2}{\partial s^2},$$

D and G are bending and shear stiffness c - damping coefficient, h - thickness of the plate. General view of the cone geometry is presented on Fig.

Consider the small end is the clamped one and the large end is free. Assuming this case, the boundary conditions are

$$u = v = w = \frac{\partial w}{\partial s} = 0, \text{ at } s = s_1 \tag{1.38}$$

$$N_s = S_{s\theta} = V_s = M_s = 0, \text{ at } s = s_2. \tag{1.39}$$

u, v, and w are the orthogonal components of displacement in the s, θ, and normal directions, respectively, $N_s, S_{s\theta}$ are the membrane forces related to the Airy stress function,V_s is the Kelvin-Kirchhoff shear, M_s is the meridional moment resultant [26].

Let us show how eigenfunctions and eigenfrequencies can be found. Consider separation of variables

$$w(t,s,\theta) = e^{i\omega t} w(s)\sin(n\theta), \tag{1.40}$$

$$F(t,s,\theta) = e^{i\omega t} F(s)\sin(n\theta). \tag{1.41}$$

We obtain for the system (1.43)(1.43)

$$\begin{pmatrix} D\widehat{a}(n) & -\widehat{b} \\ \widehat{b} & G^{-1}\widehat{a}(n) \end{pmatrix} \begin{pmatrix} w(s) \\ F(s) \end{pmatrix} = \begin{pmatrix} h\rho\omega^2 \\ 0 \end{pmatrix} \begin{pmatrix} w(s) \\ F(s) \end{pmatrix} \tag{1.42}$$

where $\widehat{a} = \left[\frac{d^4}{ds^4} + \frac{2}{s}\frac{d^3}{ds^3} - \frac{1+2n^2}{s}\frac{d^2}{ds^2} + \frac{1+2n^2}{s^2}\frac{d}{ds} - \frac{n^2(4-n^2)}{s^4}\right], \widehat{b} = \frac{1}{s\tan\alpha}\frac{d^2}{ds^2}$.

The eigenfunctions $w_{mn}(s), F_{mn}(s)$ satisfying (1.42), (1.38),(1.39) and natural frequencies ω_{mn} of the cone can be find by Galerkin's or Rayleigh–Ritz methods. Expanding the radial displacement w, and Airy function $F(t,s,\theta)$ in the series of the shallow shell eignemodes

$$w(t,s,\theta) = \sum_{mn} c_{mn}(t) w_{mn}(s) sin(n\theta), \tag{1.43}$$

$$F(t,s,\theta) = \sum_{mn} d_{mn}(t) F_{mn}(s) sin(n\theta) \tag{1.44}$$

Using that normal modes with different indexes are orthogonal we obtain equations governing the amplitudes c_{mn} as

$$\frac{\partial^2 c_{mn}}{\partial t^2} + 2\delta \frac{\partial c_{mn}}{\partial t} + (\omega^2{}_{mn}) c_{mn} = f_{mn}(t) \tag{1.45}$$

where $\delta = c/2\rho$ and ω_{nm} are frequencies of the eigenmodes.

$$f_{mn}(t) = \frac{1}{h\rho} \int \int f(t, s, \theta) w_{mn}(s) sin(n\theta) ds d\theta$$

To analyze response of the nozzle to the impact, we build finite element model of the nozzle extension using ABAQUS software package. Because the nozzle shell is much thinner than the impacting part, the later is modeled as a rigid body. We fix nozzle extension at the base and use dynamic explicit mode with general contact properties to simulate the impact. Typical results of the simulations are shown in Fig. 1.6.1(a). It can be seen from the figure that the nozzle is damaged during the impact. The damage can be characterized by two key factors: the area S of the bended part of the nozzle, and the angle of the bending. Next the geometry of the nozzle damage obtained in ABAQUS simulations is translated into the FLUENT model of the flow through the damaged nozzle and the torque amplitude induced by the flow on the damaged nozzle is estimated. As a result of this analysis we can use the inference of the impact strength to predict damage size and the torque and thrust imposed by the flow on the damaged nozzle.

To analyze in more details the nozzle damage dynamics we use the solution of Donnells equations Eq. 1.36 and Eq. 1.37 to simulate the impact-induced torque applied to the nozzle and perform computer simulation of the upper stage thrust vector control response to the impact.

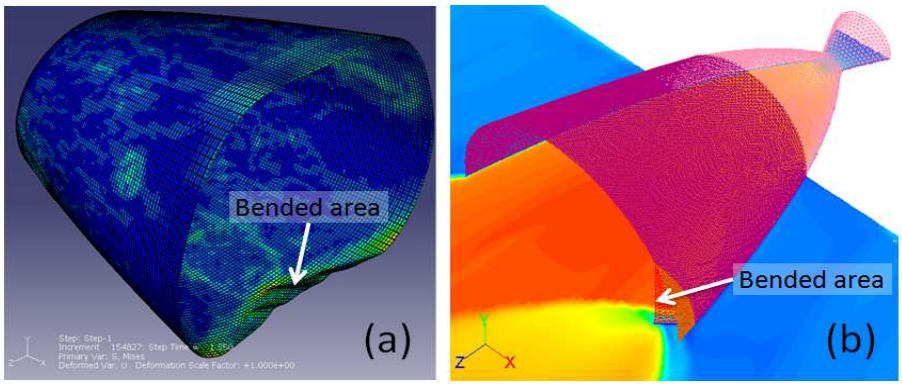

FIGURE 1.8: (a) Nozzle extension damage during stage separation failure obtained by simulations of the high-fidelity model of the nozzle extension impact in ABAQUS. (b) Predictions of the flow distribution in the damaged nozzle using FLUENT simulations.

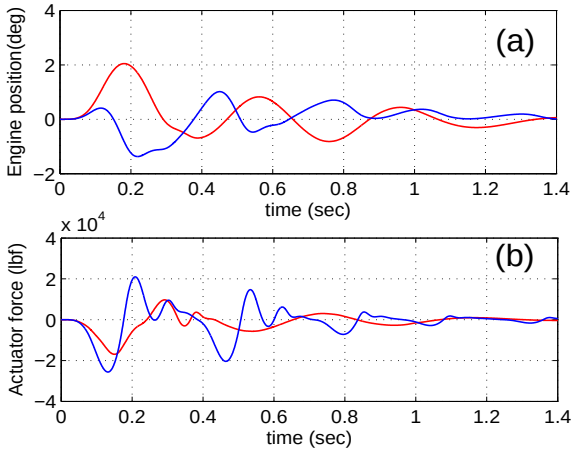

FIGURE 1.9: (a) Nozzle angular positions tilt (red) and rock (blue) during the impact. (b) Induced by the impact actuators forces components tilt (red) and rock (blue) as functions of time. (b) Induced by the impact actuators' forces components tilt (red) and rock (blue) as functions of time.

1.6.2 Second stage thrust vector control system operation simulation

Second stage thrust vector control system consists of three integrated components: turbine pump assembly, hydraulic distribution system and actuator assembly. The gas from main propulsion system starts the turbine pump assembly. Turbine pump assembly produces power for hydraulic pump. The pump circulates the fluid through the hydraulic distribution system. Two hydraulic supply strings support two actuators, which change the nozzle attitude. At nominal regime of stage separation the actuators do not operate and nozzle attitude does not change. When the first stage collides with the nozzle, the nozzle changes its angular orientation and the control system respond to the impact.

For the analysis of nozzle damage due to stage separation we use dynamic model of the vehicle second stage thrust vector control. We simulate the impact torque for a given stage separation fault and implement the impact torque into the second stage thrust vector control system simulation software. In the result of the simulation we obtain nozzle attitude changes and the actuators' forces as functions of time. The nozzle attitude changes during the impact are shown in Fig. 1.6.2(a) and the actuators' forces are shown in Fig. 1.6.2 (b).

We simulate impact torques for several separation faults, obtain impact torques for each fault and simulate thrust vector control response to each case. Different separation fault cases are described by different amplitudes of

t!]

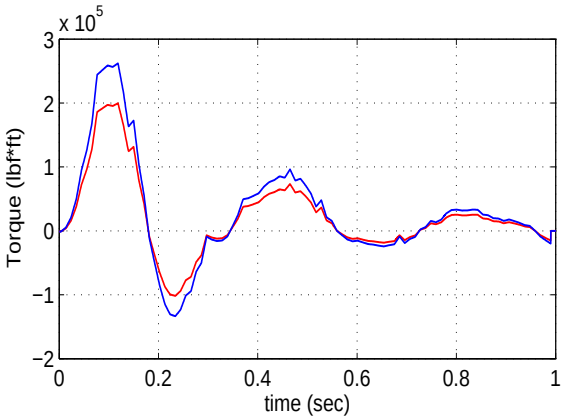

FIGURE 1.10: Actuators tilt (red) and rock (blue) torques components obtained with the MATLAB/SIMULINK simulations of the actuator forces as functions of time. These components coincide with torques components obtained in the ABAQUS simulations.

torque oscillations and, as the result, different nozzle angles and actuators forces response.

1.6.3 Diagnostics of stage separation faults

The objective of this section is to describe how we can detect separation faults and estimate nozzle damage using the second stage engine sensor data.

1-st Method: Second stage nozzle attitude analysis

We assume that we simulated several possible separation faults and obtained nozzle attitude changes for each case. If we have real time telemetry data of nozzle angular orientation in real time we can compare the telemetry data to each case from the previously simulated cases and to pick up the case of maximal correlation with the telemetry. Since we already studied the cases and estimated consequences of the impact, we can provide the prognostic of the investigated case.

2-st Method: Impact torque analysis

The second stage engine nozzle attitude changes are given by the equation

$$J\ddot{\varphi} + B\dot{\varphi} + K\varphi = Q \tag{1.46}$$

where J, B, K are the coefficients, φ is (rock/tilt) nozzle angle. The total torque applied to the nozzle $Q = Q_a + Q_c$ is the sum of the actuator torque

Q_a and the impact torque Q_c. If we know the actuator force and the nozzle angle, we can compute the impact torque with the equation

$$Q_c = J\ddot{\varphi} + B\dot{\varphi} + K\varphi - F_a \cdot l \tag{1.47}$$

where F_a is the actuator force and l is the actuator lever arm. Measuring the nozzle attitude angles φ and actuator forces F_a by the second stage engine sensors we can use the equation 1.47 and compute the impact torque applied to the nozzle extension in real time. The result of this simulation is shown in Fig. 1.6.3.

The information about impact torque behavior will allow us to estimate the nozzle extension damage and to predict the consequences of the impact. We can compare the obtained impact torque to the result of simulation for possible separation fault scenarios and choose the most probable one based on the maximal correlation of the torque Fig. 1.6.3 with the simulated cases.

It can be seen from the discussion above that the once the impact induced torque is detected the prediction of the damage is reduced to an analysis of the buckling eigenmodes of the thing conical shell that can be reduced to an analysis of a set of forced oscillators.

1.7 Normal mode expansion method dynamics for local damage detection

Metallic and composite plates are common members of airspace structures. As the size and complexity of space hardware grows, structural weight control becomes crucial. Weight requirement usually involves the use of lighter weight structures such as composites. All composite structures have one basic handicap in common: they all share a failure mechanism that is so insidious as to make it difficult to impossible to discern when and where a serious flaw may occur. The reason is that structural failures will occur internally, out of view of normal visual means of inspection. Internal de-bonds, de-laminations, cracks, and/or buckles are typical. For heavily loaded composites, such as the heavy lift launcher will undoubtedly employ, this type damage represents a major safety concern especially on man rated vehicles. The large area composite structures like Payload Shroud, the Interstage, the Core Intertank, Storage Fuel Tank, Crew Composite Modulus etc. are under broad investigation to use them in Space Vehicles. Some of the structures peculiarities of these structures you can find in reports [9, 10, 44].

In this section we report some properties of the wave propagations in plates with application to development structural health monitoring (SHM) methods. Knowing the dynamics of the structures is important for maintaining structural integrity, safety, health and IHM as whole. In this section we

by using classical Kirchhoff thin plate vibration theory will study structural properties and show how these results can be used for structural health monitoring. We will base our consideration on seminal work of Laissa (1969) where presented also references of the original papers.

1.7.1 Governing equations

Assuming the mid-surface of a plate as a reference, we shall use in-plane Cartesian coordinates. Let w be the deflection of the middle surface of the sandwich plate and than the governing differential equation of the isotropic thin plate can be presented from the classical thin plate theory. The transversely vibrating plates usually consider following equation [26]

$$D\Delta^2 w + \rho h \frac{\partial^2 w}{\partial t^2} = f(t, x, y), \tag{1.48}$$

where D is the flexural rigidity (Bending stiffness), and ρ, h are density and thickness of a plate. Operator $\Delta^2 = \nabla^2\nabla^2$ – is biharmonic operator, $f(t, x, y)$ term is lateral force per unit area responsible for external load or PZT excitation. In the case of thin homogeneous plate $D = Eh^3/12(1-\nu^2)$ is the flexural rigidity of the plate; E, ν Young's modulus, Poisson's ratio, respectively. In the case of sandwich panel stiffens is [4]

$$D = D_s = \frac{E_f t_f^3}{6} + \frac{E_c t_c^3}{12} + \frac{E_f t_f (t_f + t_c)^2}{2} = 2D_f + D_c + D_0. \tag{1.49}$$

Here Young modulus for facesheets is E_f and modulus of the core E_c , t_f and t_c are the thicknesses of the core and sheets, correspondingly. The sandwich plate has a thickness $h = 2t_f + t_c$. Each term in the right hand side is denoted by its own capital letter D, $\rho = (2\rho_f t_f + \rho_c t_c)/h$, ρ_f, ρ_c are the densities of the facesheets and the core. In expression (1.49) we have $D_f \ll D_0$, $D_c \ll D_0$.

The displacement field $w(x, y, t) = w_0 exp(i(\omega t - kx))$ describes transverse plane wave traveling in the x direction. As a result, solving (1.48) for the wavenumber we get two real roots which describe two wave propagating in opposite directions:

$$k = \pm \sqrt[4]{\omega^2 \rho h / D}, \tag{1.50}$$

while the two imaginary roots correspond to evanescent fields. The phase speed v_p of the flexural wave with frequency ω in this case is function of the plate stiffness and mass per unit area

$$v_p = \omega/k = \pm \sqrt[4]{\omega^2 D/\rho h}.$$

Let us consider generation and propagation of the flexural waves based on results of the eigenfunctions and eigenfrequencies obtained for rectangular plate. The collection of solutions for rectangular plates can be represented by deflection functions $w(x, y)$ as the product of beam functions

$$w(x,y) = \sum_m \sum_n c_{mn} X_m(x) Y_n(y), \tag{1.51}$$

where $X_m(x)$and $Y_n(y)$ are chosen as the fundamental mode shapes of beams having the boundary conditions of the plate. This choice of functions then exactly satisfies all boundary conditions for the plate, except in the case of the free edge, where the shear condition is approximately satisfied. The possible boundary conditions along the edges $x, y = 0$ and $x = L_x, y = L_y$ determine mode shapes $X_m(x), Y_n(y)$. In this case the eigenfrequencies ω are given by the formula [26]

$$\omega^2 = \frac{\pi^4 D}{L_x^4 \rho}\left[G_x^4 + G_y^4 \frac{L_x^4}{L_y^4} + 2\frac{L_x^2}{L_y^2}[\nu H_x H_y + (1-\nu) J_y J_y]\right], \tag{1.52}$$

where G, H, and J, are given functions of natural numbers determined by specific boundary conditions (Table 4.1[26]). As it was noted by Leissa there are 21 combinations of simple boundary conditions (i.e., either clamped (C), simply supported (SS), or free (F)) for rectangular plates. Frequency parameters are expressed in terms of $\omega L_x^2 \sqrt{\rho h D}$, where L_x is a length dimension. For example for SS boundary conditions for each edge we have

$$w(x,y) = 0, \text{ at } x = 0, L_x, y = 0, L_y.$$

The problem with Simply Supported edges is one of the most simplest for analytical calculation and for the rectangular plate

$$w(x,y) = \sum_m \sum_n c_{mn} \sin\left(\frac{m\pi x}{L_x}\right) \sin\left(\frac{n\pi y}{L_y}\right), \tag{1.53}$$

where L_x, L_y are the rectangular plate dimensions

$$G_x = m, H_x = J_x = m^2, G_y = n, H_y = J_y = n^2 \tag{1.54}$$

and as a result, from (1.52) we have next eigenfrequencies

$$\omega_{mn}^2 = \frac{\pi^4 D}{\rho h}\left[\left(\frac{m}{L_x}\right)^2 + \left(\frac{n}{L_y}\right)^2\right]^2, \tag{1.55}$$

where $m, n = 0, 1, 2..., m = n \neq 0$.

1.7.2 Evolution under PZT actuator

The evolution of the plate under external load can be find by considering amplitudes in equation (1.51) as a functions of t. Substituting (1.51) into

(1.48), multiplying both sides by $X_{m'}(x)Y_{n'}(y)$ and integrating over the area of the plate we obtain

$$\sum_m \sum_n [\left\{ \ddot{c}_{mn}(t) + c_{mn}\omega_{mn}^2 \right\} \int_0^{L_x} \int_0^{L_y} X_m(x)Y_n(y)X_{m'}(x)Y_{n'}(y)dxdy$$

$$= \frac{4}{L_x L_y} \int_0^{L_x} \int_0^{L_y} f(t,x,y)X_{m'}(x)Y_{n'}(y)dxdy. \tag{1.56}$$

Because the modes are orthogonal left hand side is not equal to zero only for $n = n', m = m'$. As a result, system (1.56) can be presented as system of ODE for amplitudes c_{mn}

$$\ddot{c}_{mn}(t) + \omega_{mn}^2 c_{mn}(t) = f_{mn}(t) \tag{1.57}$$

where

$$f_{mn}(t) = \frac{4}{L_x L_y} \int_0^{L_x} \int_0^{L_y} f(t,x,y)X_m(x)Y_n(y)dxdy. \tag{1.58}$$

We can easily solve the system (1.57) analytically when surface forcing is described by Dirac delta function $\delta(.)$ in space and harmonic in time. In this case

$$f(t,x,y) = \cos(\omega t)\delta(x - x_s)\delta(y - y_s),$$

where point (x_s, y_s) is the position of source term on the plate. Introducing notations

$$f_{mn}(t) = f_0(t)f_{mn}, \tag{1.59}$$

where term $f_{mn} = \frac{4}{L_x L_y} X_m(x_s)Y_n(y_s)$ determines localization of the source on the plate, and $f_0(t) = \cos(\omega t)$ we can write down the solution

$$c_{mn}(t) = c_0 \cos(\omega_{mn} t + \alpha) + f_{mn} \frac{\cos(\omega t + \beta)}{(\omega_{mn}^2 - \omega^2)}.$$

Amplitude c_0 and phase α are determined form initial conditions. Let us consider $c_{mn} = \dot{c}_{mn} = 0$, than $c_0 = -f_{mn} \frac{\cos(\beta)/\cos(\alpha)}{(\omega_{mn}^2 - \omega^2)}$ and solution for amplitudes and phase are

$$c_{mn}(t) = \frac{f_{mn}}{(\omega_{mn}^2 - \omega^2)} \left[\cos(\omega t + \beta) - \frac{\cos\beta}{\cos\alpha} \cos(\omega_{mn} t + \alpha) \right]. \tag{1.60}$$

$$\alpha = \tan^{-1} \left[\frac{\omega}{\omega_{mn}} \tan(\beta) \right]. \tag{1.61}$$

Solution evidently explains one of the possible ways of SHM. The denominator

is equal to zero at $\omega = \omega_{mn}$ which corresponds to resonances of the plate. Any structural defects will change ω_{mn} and by sweeping frequency ω we can determine shift of ω_{mn}.

Let us consider next example when pulse is presented by the form [25]

$$f_0 = e^{-t/\tau} \cos \omega t. \tag{1.62}$$

The excitation signal (1.62) makes it possible to present solution of the system as [25]

$$\begin{aligned} c_{mn} &= f_{mn} \frac{\varpi_{mn}^2 \cos \omega_{mn} t + (\tau \omega_{mn})^{-1} (\varpi_{mn}^2 + 2\omega^2) \sin \omega_{mn} t}{\varpi_{mn}^4 + 4\omega^2/\tau^2} \\ &\quad + f_{mn} e^{-t/\tau} \frac{\varpi_{mn}^2 \cos \omega t - 2(\omega/\tau) \sin \omega t}{\varpi_{mn}^4 + 4\omega^2/\tau^2} \end{aligned} \tag{1.63}$$

where $\varpi_{mn}^2 = \omega_{mn}^2 + 1/\tau^2 - \omega^2$.

Let us consider how wave propagating from point source can interact with local damage.

1.7.3 Model of the damage

Local stiffness reduction can be caused by different faults. The loss of bending stiffness can be caused by debond, delamination, honeycomb crash or reduction of the modulus of facesheet due to impact. Any of these structural failures will lead to change of the stiffness and mass parameters. As a result in framework of plate theory we can generalize damage as domain with different structural properties than rest of the plate.

Let us consider damage model as a decrease in structural local stiffness by function $g(x-x_d, y-y_d)$ which reflects changes in the local structural material elastic coefficients. Term in the left-hand side of equation (1.48) is modified

$$Dg(x - x_d, y - y_d)\Delta^2 w + \rho h \frac{\partial^2 w}{\partial t^2} = f(t, x, y), \tag{1.64}$$

where function describing damage is centered $g(x - x_d, y - y_d)$ at the certain point (x_d, y_d) characterizing local change in stiffness. We transform equation (1.64) to the form

$$D\Delta^2 w + \rho h \frac{\partial^2 w}{\partial t^2} = \varepsilon f(t, x, y) + D\varepsilon(x, y)\Delta^2 w, \tag{1.65}$$

where right hand side value $\varepsilon(x, y) = 1 - g(x - x_d, y - y_d)$ is not equal to zero in a small domain of the damage.

Considering that the value $\varepsilon(x, y)$ in (1.65) is sufficiently small we can apply perturbation technique: we find the solution for $\varepsilon(x, y) = 0$ and then substitute displacement in right hand side in the expansion through normal modes form (1.51). In this case damage term works like a source of secondary waves generated in the structure.

Applying the same procedure of the expansion solutions system of equations for mode amplitudes is

$$\ddot{c}_{mn}(t) + c_{mn}(t)\omega_{mn}^2 = f_{mn}(t) + \varepsilon\Lambda_{mn}(x_d, y_d). \tag{1.66}$$

where for calculation of the term $\varepsilon\Lambda_{mn}$

$$\varepsilon\Lambda_{mn} = \frac{4}{L_x L_y}\sum_{k,l}\int_0^{L_x}\int_0^{L_y}\varepsilon(x,y)\omega_{kl}^2 c_{kl}X_m(x)Y_n(y)X_{m'}(x)Y_{n'}(y)dxdy \tag{1.67}$$

we have to know exact distribution of the value $\varepsilon(x, y)$

As a result, we obtain solution for transverse displacement $w(x, y, t)$ which can be presented as

$$\begin{aligned} w(x,y,t) = \sum_{m,n=1}^{N_x,N_y} &\{c_{mn}(t) + \varepsilon\Lambda_{mn}(x_d,y_d)\left[1-\cos(2\omega t)\right]\}\times \\ &\sin\left(\frac{m\pi x}{L_x}\right)\sin\left(\frac{n\pi y}{L_y}\right), \end{aligned} \tag{1.68}$$

where $c_{mn}(t)$ is determined by expression(1.63) and $\varepsilon\Lambda(x_d, y_d)_{mn}$.

In order to calculate (1.67) we consider $c_{kl}(t)$ at the damaged region as a given from solution for $\varepsilon = 0$. Let us consider simplest model of damage when in local square we have a reduced stiffness by value $\varepsilon = const$

$$\varepsilon(x,y) = \begin{cases} \varepsilon & \text{for } x_d - D \le x \le x_d + D, x_d - D \le y \le x_d + D, \\ 0 & \text{for the rest of the plate.} \end{cases} \tag{1.69}$$

In the case of simply supported boundary conditions we have sine eigenfunctions (1.53) and damaged term in (1.66) can be expressed as

$$\varepsilon\Lambda_{mn}(x_d, y_d) = \frac{\sum\limits_{k,l}\omega_{kl}^2 c_{kl}}{\pi^2 L_x L_y \omega_{mn}^2}[a_{km}(x_d) - a_{km}(y_d)][a_{ln}(x_d) - a_{ln}(y_d)], \tag{1.70}$$

where $a_{km}(x_d) = \frac{1}{k-m}\sin(k-m)\frac{\pi x}{L_x}|_{x_d-d}^{x_d+d}$, $a_{km}(y_d) = \frac{1}{k+m}\sin(k+m)\frac{\pi y}{L_y}|_{y_d-d}^{y_d+d}$, $a_{ln}(x_d) = \frac{1}{(l-n)}\sin(l-n)\frac{\pi x}{L_x}|_{x_d-d}^{x_d+d}$, $a_{ln}(y_d) = \frac{1}{(l+n)}\sin(l+n)\frac{\pi y}{L_y}|_{y_d-d}^{y_d+d}$.

Solution is given by (1.68) and these results are plotted on figure 1.11 a) and b) where first graph represent total solution and plot (b) reflects a difference in displacements for healthy structure and damaged one.

For computer simulation the force excitation point S is kept fixed at the center of the plate $(L_x/2, L_y/2)$ and the damage is located at certain distance (point x_d, y_d) from the corner $(0, 0)$. Some of the results for transverse displacement are plotted in figure 1.12 as a function of (x, y) for different value of t and the simply supported boundary conditions along the edges. In the simulation we used Hanning windowed signal with number of pulses N

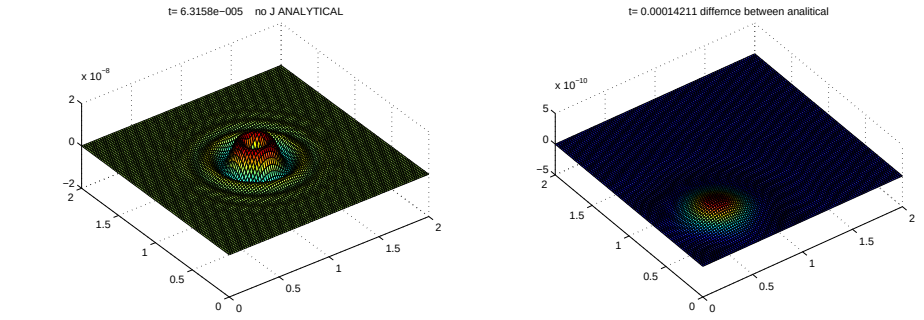

(a) (b)

FIGURE 1.11: Analytical solution for w out of plane displacement for: $t = 0.0002sec$ – (a), and difference between the damaged and pristine signal – (b)($x_d = y_d = 0.5m$, $d = 0.025m$, $x_s = y_s = 1m$, $L_x = L_y = 2m$, $N_x = N_y = 20$, Input signal is determined by formula (1.63), $\tau = 0.00001sec$, $f = 10kHz$, $\varepsilon = 0.1$, $\omega = 2\pi f$. Structural parameters are $E_f = 10^{11}Pa$, $\rho_f = 1580kg/m^3$, $\rho_c = 110kg/m^3$, $E_c = 2 \cdot 10^8 Pa$, $t_c = 0.03m$, $t = 0.003m$.

$$f_0(t) = \begin{cases} \sin\left(\frac{\omega}{N}t\right)\sin\left(\omega t\right), & \text{for } t \le t_0 = N\pi/\omega, \\ 0, & \text{for } t > t_0. \end{cases}$$

where ω is the central frequency and signal is comprised of component waves over a close range of this frequency. Changing of the base frequency ω changes the wavenumber (1.50) and wavelength of the excitation signal. The influence of a local change in stiffness (different stiffness for the size 5 cm) on the propagation of flexural waves is considered. The simulation was made for a different number of the modes N_x, N_y. The mode number affects the accuracy of calculation. We simulated the structure till reflection from the boundaries is negligible. By increasing time of simulation incident pulse interfere with reflected one and patterns of wave distribution are much more complicated. The local stiffness lost changes the amplitude of the scattered signal but does not change general picture. We can observe that damaged region plays the role of the scatterer generating scattering waves.

For the example expressed by (1.68) two distributions are plotted just to show evolution of field $w(x, y)$. Clear indication of damage was shown for the time when wave reaches the damaged region (Figure 1.12c). The difference in the $w(x, y)$ between the damaged and pristine signal is depicted in Figure 1.12d).(distribution $w(x, y)$ without first term in (1.68)). This makes it possible to characterize the damage.

This study clearly shows that normal mode expansion method is capable of

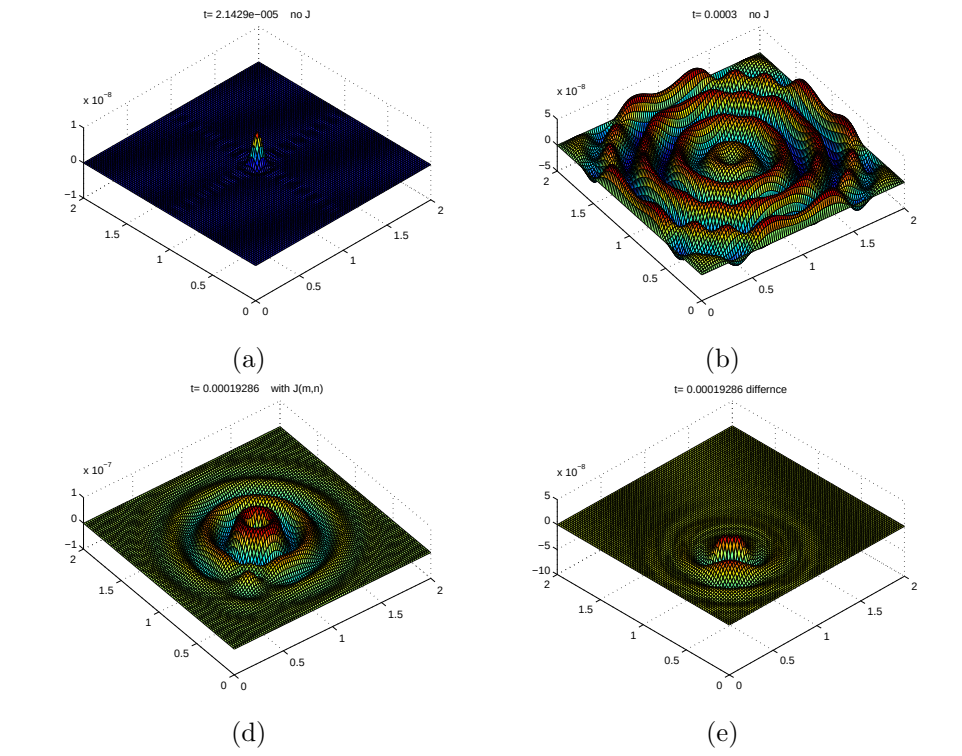

FIGURE 1.12: Out of plane displacement $w(x, y)$ at $t = 2 \cdot 10^{-5} sec$- (a), $t = 3 \cdot 10^{-4} sec$– (b) for nondamaged plate, for damaged one at $t = 2 \cdot 10^{-4} sec$– (c) and difference between the damaged and pristine value of $w(x, y)$at $t = 2 \cdot 10^{-4} sec$– (d). Input signal is Hanning windowed signal with $N = 3.5$, $f = 10kHz$, Structural parameters are $E_f = 10^{11} Pa$, $\rho_f = 1580 kg/m^3$, $\rho_c = 110 kg/m^3$,$E_c = 2 \cdot 10^8 Pa$, $t_c = 0.03m$, $t_f = 0.003m$.

capturing the physics of wave propagation in plate structures. We see a scattering pattern which in general closely resembles that interaction of wave with damaged region. Using the results obtained earlier, it is analytically shown and verified by computer simulation that the normal function expansion method describes damage state of the plate by changing the evolutionary dynamics of several modes. As a result, dynamic inference method is very promising for SHM of the plates. Taking into account large number of eigenmode expansion increases the accuracy but at least ten terms is sufficient to grasp main characteristic features of the damage presented in the plate.

1.8 Dynamical inference of a set of coupled oscillators

It was shown that several important problems of the IHM in aerospace applications render themselves into a set of coupled stochastic differential equations ideally suited for analysis in the framework of dynamical inference. Specifically, we show that an open problem of the SHM for an on-board detection of the stage separation failure and damage in composite materials can be reduced to the DI of a set of oscillators representing the dynamics of the amplitudes of the eigenmodes. In fact, fast online DI of a set of oscillators with time varying parameters is of particular importance across a wide range of interdisciplinary applications including e.g. neurophysiology [30] and active control of combustion instability in liquid motors [7].

1.8.1 General inferential framework for a set of coupled oscillators

In this section, we briefly outline a general framework for a dynamical inference of such sets of oscillators. We consider a system of equations in the form system in the form

$$\begin{aligned} &\dot{v}_j = \alpha_j v_j + b_j v_j^2 + c_j v_j^3 - q_j + \eta_j + \sqrt{D_{ij}}\,\xi_j, \\ &\dot{q}_j = -\beta\, q_j + \gamma_j\ v_j, \\ &\langle \xi_j(t)\,\xi_i(t')\rangle = \delta_{i\,j}\,\delta(t-t'), \quad j = 1:L. \end{aligned} \tag{1.71}$$

The system (1.71) represents a dynamics of L nonlinear oscillators with coordinates q_j and velocities v_j driven by random force with components ξ_j, which are mixed by a diffusion matrix with elements D_{ij}. This form of equations that can model a wide range of nonlinear phenomena (see e.g. [5]) and can be reduced, in particular, to a set of linear oscillators obtained in previous two sections un the context of online SHM problem.

In practice, the measurements of the dynamical variables $v_j(t)$ is a separate important problem in each specific application. in this example we use a

measurement model in a form of measurement matrix X, which is frequently found in theory of dynamical inference,

$$y_i \;=\; X_{ij}\, v_j\,. \tag{1.72}$$

Here y_i are measured variables, which are related to v_j by linear transformation with an *unknown* matrix X. All the accessible information is contained in y_i. The problem is, therefore, to learn model parameters $\mathcal{M} = \{\eta_i, \alpha_i, q_i(0), \gamma_i, D_{ij}, X_{ij}\}$ from time series data $\{y_i\}$.

To develop a general inferential framework for a solution of this problem we notice that the second linear ordinary differential equation in Eqs. (1.71) connecting coordinates and velocities can be integrated explicitly (see [30, 16]) to obtain

$$q_j(t) = \gamma \int_0^t d\tau e^{-\beta\,(t-\tau)} v_j(\tau) + e^{-\beta\,t} q_j(0). \tag{1.73}$$

On substituting (1.73) into the first equation in (1.71) we have

$$\begin{aligned} &\dot{v}_j = \alpha_j v_j + b_j v_j^2 + c_j v_j^3 + \eta_j \\ &- \gamma_j \int_0^t d\tau e^{-\beta\,(t-\tau)} v_j(\tau) - e^{-\beta\,t} q_j(0) + \sqrt{D_{ij}}\xi_j, \end{aligned} \tag{1.74}$$

Here $j = 1, ..., L$ and $q_j(0)$ is a set of initial coordinates for unobservable variable $q_j(t)$. Thus the reconstruction of unobservable variables $q_j(t)$ is reduced to inference of L initial conditions $q_j(0)$.

Variables $v_j(t)$ can also be excluded from further consideration by using eq. (1.72). Indeed, on substituting $v = X^{-1}y$ into (1.74) we obtain in vector notations:

$$\begin{aligned} \dot{y} = X\alpha\left(X^{-1}\,y\right) + Xb\left(X^{-1}\,y\right)^2 + Xc\left(X^{-1}\,y\right)^3 + e^{-\beta\,t} X q_0 \\ - \int_0^t e^{\beta(t-\tau)} X\gamma\left(X^{-1}\,y\right) d\tau + X\eta + X\sqrt{D}\xi(t), \end{aligned} \tag{1.75}$$

where α, b, and c are vectors with components $\{\alpha_j\}$, $\{b_j\}$, and $\{c_j\}$ respectively, $q_0 = q(t=0)$ and

$$\left(X^{-1}\,y\right)^n = \begin{pmatrix} \left(\sum_{i=1}^L \tilde{x}_{1i} y_i\right)^n & \dots & 0 \\ \vdots & \ddots & \vdots \\ 0 & \dots & \left(\sum_{i=1}^L \tilde{x}_{Li} y_i\right)^n \end{pmatrix}.$$

The Eq. (1.75) can be rewritten in a more general form

$$\begin{aligned} &\dot{y}_i = \tilde{\alpha}_{ij}\, y_j + \tilde{b}_{ijk}\, y_j\, y_k + \tilde{c}_{ijkl}\; y_j\, y_k y_l + \tilde{\eta}_i + \\ &-\Phi_i \tilde{\gamma}_{il} y_l - e^{-\beta\,t}\, \tilde{z}_i + \sqrt{\tilde{D}_{ij}}\xi_j(t), \end{aligned} \tag{1.76}$$

where the meaning of the parameters with $\sim$ is clear from the comparison of (1.75) and (1.77), see also [30, 16].

Note that presentation (1.75) covers the whole model space of a set of coupled nonlinear oscillators with polynomial base functions of the power 3. This presentation can also be viewed as an independent model for inferring unknown parameters of a system of coupled nonlinear oscillators in the case when oscillators velocities y_i can be measured directly.

To infer the set of unknown parameters

$$\tilde{\mathcal{M}} = \{\tilde{\eta}_i, \tilde{\alpha}_{ij}, \tilde{b}_{ijk}, \tilde{c}_{ijkl}, \tilde{\gamma}_{ij}, \tilde{z}_i, \tilde{D}_{ij}\}$$

of the system (1.77) of L coupled oscillators (1.75) within our inferential framework 1.2 one can introduce the following base functions

$$\begin{aligned}\phi(x) = \{&1, y_1, ..., y_L, y_1^2, y_1y_2, ..., y_1y_L, y_2^2, y_2y_3, ..., y_2y_L, ..., y_1^3,\\ &y_1^2y_2, ..., y_1^2y_L, y_2^3, y_2^2y_1, ..., y_2^2y_L, ..., y_L^2y_{L-1}\,, y_L^3\,, \Phi_1, ..., \Phi_L\,, e^{-\beta t}\}\end{aligned} \tag{1.77}$$

where $\Phi_i \equiv \int_0^t y_i(\tau)e^{\beta(\tau-t)}$.

The total number of unknown parameters is $N_{tot} = (2 + 2L + L^2)L + L(L+1)^2/2$ and is increasing as L^3 with the dimension of the system. These parameters can be inferred directly from (1.77) using Eqs. (1.8) – (1.11) is the measurement matrix is known. In the case of unknown measurement matrix one has to infer additional L^2 coefficient of unknown matrix X_{ij}, which is not symmetric in general. To solve this problem we notice that in practice the number of the coefficients of the original system is always significantly smaller then the full set of equations N_{tot}, because of the symmetry, which is always present in real systems. For example, for the sets of linear oscillators that appear in eigemode expansion of the SHM problem in the on-board analysis of stage separation failure and damage of the composite materials the 2^{nd} equation in (1.71) has the form $\dot{q}_j = v_j$, i.e. $\beta = 0$, $\gamma_j \equiv 1$, and all $\tilde{b}_{ijk}$ and $\tilde{c}_{ijkl}$ are also zero. Furthermore, the eigenfrequencies of expansion in eigenmodes of every specific structural component that requires on-board SHM must be learned beforehand from extensive preliminary ground and in-flight tests, which significantly simplifies the problem.

1.8.2 Numerical example

We now consider a numerical example with a $2D$ set of oscillators (1.74) where all the coefficients of (1.74), but β are assumed unknown together with unknown coefficients of the measurement matrix $\{x_{ij}\}$. In 2D case the set $\tilde{\mathcal{M}}$ of variables of the transformed dynamics (1.75) corresponds to the following set of the base functions

$$\phi(x) = \{1\,,\, y_1\,,\, y_2\,,\, y_1^2\,,\, y_2^2\,,\, y_1y_2\,,\, y_1^3\,, y_1^2y_2\,,\, y_1y_2^2\,,\, y_2^3\,,\, \Phi_1\,,\, \Phi_2\,,\, e^{-\beta t}\}.$$

In general it should be possible to reconstruct all unknown coefficients of the original system for any number of FHN oscillators as long as we can establish

the connection between the set $\tilde{\mathcal{M}}$ and the set of original unknown variables of (1.71)

$$\mathcal{M} = \{\eta_i, \alpha_i, b_i, c_i, \gamma_i, q_i(0), D_{ij}, X_{ij}\}$$

Here we introduce explicit relations for the case $L = 2$.

$$X^{-1}\begin{bmatrix}\eta_1\\ \eta_2\end{bmatrix} = \begin{bmatrix}\tilde{\eta}_1\\ \tilde{\eta}_2\end{bmatrix}, \qquad \begin{bmatrix}q_{0,1}\\ q_{0,2}\end{bmatrix} = X^{-1}\begin{bmatrix}\tilde{q}_1\\ \tilde{q}_2\end{bmatrix}, \qquad \tilde{D}X^{-1} = X^{-1}D. \tag{1.78}$$

$$\begin{bmatrix}\gamma_1 & 0\\ 0 & \gamma_2\end{bmatrix} X^{-1} = X^{-1}\begin{bmatrix}\tilde{\gamma}_{11} & \tilde{\gamma}_{12}\\ \tilde{\gamma}_{21} & \tilde{\gamma}_{22}\end{bmatrix}, \tag{1.79}$$

$$\begin{bmatrix}\alpha_1 & 0\\ 0 & \alpha_2\end{bmatrix} X^{-1} = X^{-1}\begin{bmatrix}\tilde{\alpha}_{11} & \tilde{\alpha}_{12}\\ \tilde{\alpha}_{21} & \tilde{\alpha}_{22}\end{bmatrix}, \tag{1.80}$$

The unknown elements x_{ij} of the inverse measurement matrix X^{-1} and parameters with tilde are the model parameters of the transformed system (1.75) that can be inferred directly using time series data $\{y_i\}$. Relations (1.78)-(**??**) allows one to reconstruct 15 unknown parameters of the original system, including elements of the noise and measurement matrixes. Note, however, that coefficients $(1+\alpha_i)$ can also be assumed unknown in general and the following relations can be used to reconstruct them

$$\begin{bmatrix}1+\alpha_1 & 0\\ 0 & 1+\alpha_2\end{bmatrix}\begin{bmatrix}x_{11}^2 & 2x_{11}x_{12} & x_{12}^2\\ x_{21}^2 & 2x_{21}x_{22} & x_{22}^2\end{bmatrix} = X^{-1}\begin{bmatrix}\tilde{b}_{111} & \tilde{b}_{112} & \tilde{b}_{122}\\ \tilde{b}_{211} & \tilde{b}_{212} & \tilde{b}_{222}\end{bmatrix}, \tag{1.81}$$

Similarly, the relation between the coefficients for polynomials of power 3 are given by

$$\begin{bmatrix}-1 & 0\\ 0 & -1\end{bmatrix}\begin{bmatrix}x_{11}^3 & 2x_{11}^2x_{12} & 2x_{11}x_{12}^2 & x_{12}^3\\ x_{21}^3 & 2x_{21}^2x_{22} & 2x_{21}x_{22}^2 & x_{22}^3\end{bmatrix} = X^{-1}\begin{bmatrix}\tilde{c}_{111} & \tilde{c}_{112} & \tilde{c}_{121} & \tilde{c}_{122}\\ \tilde{c}_{211} & \tilde{c}_{212} & \tilde{c}_{221} & \tilde{c}_{222}\end{bmatrix}, \tag{1.82}$$

We now analyze the convergence of the method in the case when all the parameters of the reduced model (1.75), including elements of the measurement matrix are unknown. The sampling rate was 35 kHz, we used 9 blocks of data with 5000 points in each block, and these block of data were generated at random 1000 time to analyze the statistics of the convergence.

To reconstruct both the mixing matrix X and the parameters of the original system $\mathcal{M}$ from the inferred parameters $\tilde{\mathcal{M}}$ of the transformed system (1.75) we have to solve equations (1.78–1.82) with respect to elements of $\tilde{\mathcal{M}}$. In a particular case of transformation given in a simple form of Eqs. (1.78–1.82) the solution of this problem can be found using standard nonlinear least square method [8], however, an additional optimization over the set of initial values may be required. We stress that the present technique is not restricted to the 2D case and can be employed in the general case of L oscillators.

The results of the inference of the transformed and original parameters

TABLE 1.5: Values of some of the transformed and original coefficients inferred using 30000 points obtained from measurement matrix and real parameters reconstruction. The actual values (second column) are compared with the inferred values (third column), relative errors are given in the last column.

Parameter	Actual Value	Estimate	Error
$\tilde{\eta}_1$	0.9200	0.924384	0.022624
$\tilde{\eta}_2$	0.3500	0.351001	0.009063
$\tilde{b}_{222}$	1.7550	1.758011	0.037047
$\tilde{b}_{112}$	-2.1086	-2.114731	0.068268
X_{11}	1.7	1.686459	0.796526
X_{12}	0.8	0.794263	0.717092
X_{21}	0.2	0.196746	1.626811
X_{22}	0.9	0.898222	0.197610
η_1	0.4	0.406227	1.556788
η_2	0.3	0.302462	0.820660
α_1	-0.35	-0.351992	0.569082
α_2	-0.2	-0.200376	0.188228
b_1	1.35	1.357427	0.550145
b_2	1.2	1.203863	0.321885
c_1	-1.0	-0.999520	0.047957
c_2	-1.0	-0.999114	0.088582

of a set of oscillators are summarized in Tab. **??**. It can be seen from the table that the DI method allows us to reconstruct both the elements of the measurement matrix and the parameters of the transformed (1.77) and original (1.74) systems. Our analysis shows that the relative error of inference better then 2% is achieved in less then 1 sec of measurements.

We, therefore, conclude that the general inferential framework for a set of coupled oscillators provided by Eqs. (1.8) – (1.11), (1.77) – (1.77) is one of the primary candidates for on-board SHM in aerospace applications.

1.9 Conclusion

It was shown that several important applications of IHM in aerospace render themselves into a problem of on-line inference a set of coupled stochastic differential equations. A convenient approach to a solution of this problem was introduced within the framework of dynamical inference. It was shown that in a wide range of practical cases this problem can be solved analytically using path-integral approach to the maximum likelihood estimation. the robustness of the solution in the presence of strong dynamical noise was demonstrated in

application to the inference of archetypal nonlinear stochastic Lorenz system. The ability of the method to infer simultaneously discrete and continuous parameters was further illustrated by the application of the DI to the fast on-line estimation of parameters and detection of leaks in stochastic hybrid three tank system, which standard engineering control benchmark. the later problem was considered in a specific context of ground support system for liquid fuel filling system.

In the remaining part of the chapter a progress in development of some selected FD&P systems for in-flight structural health monitoring was discussed. In the first example a dynamical model of the SRM ballistics in nominal and off-nominal regimes was presented. It was shown that the DI approach can be used to detect abrupt fault-induced changes in the parameters of the SRM. It was shown further that the DI method can be used to reduce the probability of "misses" in detection of the SRM faults on-board by inferring coefficients of the diverging terms in polynomial fit to small deviations of pressure from the nominal regime and generating an earlier warning when the inference results begin to converge.

In the next example a progress in development of in-flight diagnostic and prognostic system for stage separation failure was considered. A mathematical formulation of the problem of structural dynamics of a truncated cone under unsymmetrical unsteady load due to impact was given that provides estimates for the stresses required for nozzle extension buckling. The results of the high-fidelity simulations in ABAQUS confirmed the buckling scenario and allowed to establish correlation between the strength of the impact induced torque and the damage of the nozzle. The model of the thrust vector control was used to predict the tilt/rock angles and forces generated by the TVC in response to impact. A dynamical analysis of these forces allows one to build FD&P system for stage separation failure and to cast the problem in terms of the DI of a set of driven oscillators representing amplitudes of the nozzle extension eigenmodes.

In the third example a problem of in-flight structural health monitoring of composite sandwich plate was analysed. It was shown that normal mode expansion method is capable of capturing the physics of wave propagation in plate structures and may describe damage state of the plate. As a result, dynamic inference method is very promising for SHM of the plates. It was demonstrated in this context that it is sufficient to keep in the expansion up to ten terms to grasp main characteristic dynamical features corresponding to the damage present in the plate.

Finally, the a general inferential framework for fast on-line reconstruction of the parameters of a set of coupled oscillators was presented in the context of the SHM problem. It was shown that the method allows for an accurate reconstruction of the system parameters even when the velocities of teh oscillators are mixed by the linear measurement matrix with unknown elements and coordinates of the oscillators are not accessible for measurements. We

concluded that the DI is one of the primary candidates for on-board SHM in aerospace applications.

Ultimately IHM research will yield integrated, multi-disciplinary analysis and optimization capabilities that enable system-level designs providing graceful recovery from in-flight failures, computationally efficient tools for in-flight prognosis of aircraft health including integrated predictive and sensor capabilities, and preventative and adaptive systems for in-flight operability and informed logistics and maintenance.

Bibliography

[1] `http://www.simulia.com/`.

[2] `http://www.ansys.com/`.

[3] *Dynamics and Thermodynamics of Solid-Propellant Rockets*. Wiener Bindery Ltd., 1967.

[4] *The Handbook of Sandwich Construction*. EMAS Ltd, 1997.

[5] Analytical approach to the stochastic fitzhugh-nagumo system and coherence resonance. 60(6):7270–7276, 1999.

[6] Design reliability comparison for spacex falcon vehicles. Technical report, Futron Corporation, 2004. `http://www.spacex.com/FutronDesignReliability.pdf`.

[7] A. Annaswamy and A. Ghoniem. Active control of combustion instability: Theory and practice. *IEEE Control Systems Magazine*, 22(6):37–54, 2002.

[8] D. M. Bates and D. G. Watts. *Nonlinear Regression and Its Applications*. Wiley, New York, 1988.

[9] B. A. Bednarcyk, S. M. Arnold, C. S. Collier, and P. W. Yarrington. Preliminary structural sizing and alternative material trade study for cev crew module. In *48th AIAA/ ASME/ ASCE/ AHS/ASC Structures, Structural Dynamics, and Materials Conference*, Honolulu, HI, April 2007.

[10] B. A. Bednarcyk, S. M. Arnold, and D. A. Hopkins. Design of fiber reinforced foam sandwich panels for large ares v structural applications. In *51st AIAA/ASME/ASCE/AHS/ASC Structures, Structural Dynamics, and Materials Conference*, pages 1–19, Orlando, FL, April 2010.

[11] C. L. Bremer and D. T. Kaplan. Markov chain monte carlo estimation of nonlinear dynamics from time series. *Physica D*, 160:116–126, 2001.

[12] W.G. Brownlee. *An Experimental Investigation of Unstable Combustion in Solid Propellant Rocket Motors*. PhD thesis, Dissertation, California Institute of Technology, 1959.

[13] S. Cauchemez and N. M. Ferguson. Likelihood-based estimation of continuous-time epidemic models from time-series data: application to measles transmission in london. *Journal of the Royal Society Interface*, 5(25):885–897, 2008.

[14] J. Christensen-Dalsgaard. Helioseismology. *Rev. Mod. Phys.*, 74(4):1073–1129, 2002.

[15] P. Congdon. *Bayesian statistical modelling*. Wiley series in probability and statistics. Wiley, Chichester, 2001.

[16] A. Duggento, D. G. Luchinsky, V. N. Smelyanskiy, I. A. Khovanov, and P. V. E. McClintock. Inferential framework for nonstationary dynamics. ii. application to a model of physiological signalling. *Phys. Rev. E*, 77:061106, 2008.

[17] M. I. Dykman. Large fluctuations and fluctuational transitions in systems driven by colored gaussian noise–a high frequency noise. *Phys. Rev. A*, 42:2020–2029, 1990.

[18] D. J. D. Earn, S. A. Levin, and P. Rohani. Coherence and conservation. *Science*, 290(5495):1360–1364, 2000.

[19] J.-M. Fullana and M. Rossi. Identification methods for nonlinear stochastic systems. *Physical Review E*, 65:031107, 2002.

[20] J. Gradisek, S. Siegert, R. Friedrich, and I. Grabec. Analysis of time series from stochastic processes. *Phys. Rev. E*, 62(3):3146–3155, 2000.

[21] R. Graham. Path integral formulation of general diffusion processes. *Z. Phys. B*, 26:281–290, 1977.

[22] J. P. M. Heald and J. Stark. Estimation of noise levels for models of chaotic dynamical systems. *Phys. Rev. Lett.*, 84(11):2366–2369, 2000.

[23] E. L. Ionides, C. Breto, and A. A. King. Inference for nonlinear dynamical systems. *Proceedings of the National Academy of Sciences*, 103(49):18438–18443, 2006.

[24] H. Jeffreys. *Theory of Probability*. Clarendon Press, Oxford, 3-rd edition, 1961.

[25] L. D. Landau and E. M. Lifshitz. *Mechanics*. Pergamon, London, 1976.

[26] A.W. Leissa. Vibration of plates. Technical report, 1969.

[27] A.S. Lincon, D. Sivakumar, and J. Prakash. State and fault parameter estimation applied to three-tank bench mark relying on augmented state kalman filter. 9:34–41, 2007.

[28] D. G. Luchinsky, M. M. Millonas, V. N. Smelyanskiy, A. Pershakova, A. Stefanovska, and P. V. E. McClintock. Nonlinear statistical modeling and model discovery for cardiorespiratory data. *Physical Review E*, 72(2):021905, 2005. Part 1 021905.

[29] D. G. Luchinsky, V. V. Osipov, V. N. Smelyanskiy, I. Kulikov, A. Patterson-Hein, B. Hayashida, M. Watson, D. Shook, M. Johnson, S. Hyde, and J. Shipley. *Aerospace Technologies Advancements*, chapter Integrated Vehicle Health Management for Solid Rocket Motors, pages 259–290. INTECH, 2010. `http://sciyo.com/books/show/title/aerospace-technologies-advancements?PHPSESSID=4limatdbk6le2po0e36cdn45c6`.

[30] D. G. Luchinsky, V. N. Smelyanskiy, A. Duggento, and P. V. E. McClintock. Inferential framework for nonstationary dynamics part i: Theory. *Phys. Rev. E*, 77:061105, 2008.

[31] D.G. Luchinsky, V.V. Osipov, V.N. Smelyanskiy, A. Patterson-Hine, B. Hayashida, M. Watson, J. McMillin, D. Shook, M. Johnson, and S. Hyde. Model-based diagnostics and prognostics for solid rocket motors. In *Annual Conference of the Prognostics and Health Management Society, 2009 PHM*, 2009.

[32] J.E. McMillin. Scaling equations for ballistic modeling of solid rocket motor case breach. In *42nd AIAA/ASME/ SAE/ASEE Joint Propulsion Conference and Exhibit*, 2006.

[33] P. E. McSharry and L. A. Smith. Better nonlinear models from noisy data: attractors with maximum likelihood. *Physical Review Letters*, 83:4285–4288, 1999.

[34] R. Meyer and N. Christensen. Bayesian reconstruction of chaotic dynamical systems. *Physical Review E*, 62:3535–3542, 2000.

[35] R. Meyer and N. Christensen. Fast bayesian reconstruction of chaotic dynamical systems via extended kalman filtering. *Phys. Rev. E*, 65:016206, 2001.

[36] V. V. Osipov, D. G. Luchinsky, V. N. Smelyanskiy, S-H. Lee, C. Kiris, and D. A. Timucin. Bayesian framework for in-flight srm data management and decision support bayesian framework for in-flight srm data management and decision support. In Dmitry G. Luchinsky, editor, *Aerospace Conference, 2007 IEEE*, pages 1–16, 2007.

[37] V.V. Osipov, D.G. Luchinsky, V.N. Smelyanskiy, and D.A. Timucin. Case breach fault model and diagnostic for the solid rocket. AIAA 2007-5823, 2007. 43rd AIAA/ASME/SAE/ASEE Joint Propulsion Conference & Exhibit, 8 - 11 July 2007, Cincinnati, OH.

[38] Ann Patterson-Hine, Gordon Aaseng, Gautam Biswas, Sriram Narasimhan, and Krishna Pattipati. A review of diagnostic techniques for ishm applications. 2008. `http://citeseerx.ist.psu.edu/viewdoc/summary?doi=10.1.1.118.953`.

[39] M. Sailta. Verification of spatial and temporal pressure distribution in segmented solid rocket motors. In *27th Aerospace Science Meeting, 1989 AIAA*.

[40] M. Salita. Modern srm ignition transient modeling. i - introduction and physical models. In *37th AIAA/ASME/SAE/ASEE Joint Propulsion Conference and Exhibit, 2001 AIAA*, 2001.

[41] C. Seife. Space shuttle: Columbia disaster underscores the risky nature of risk analysis. *Science*, 2003.

[42] M. Siefert, A. Kittel, R. Friedrich, and J. Peinke. On a quantitative method to analyze dynamical and measurement noise. *Europhys. Lett.*, 61(4):466–472, 2003.

[43] S. Siegert, R. Friedrich, and J. Peinke. Analysis of data sets of stochastic systems. *Phys. Lett. A*, 253:275–280, 1998.

[44] D. W. Sleight, D. Paddock, J. Jeans, and J. Hudeck. Structural design and analysis of the upper pressure shell section of a composite crew module. In *11th ASCE Aerospace Division International Conference (Earth and Space 2008)*, Long Beach, CA, 2008.

[45] V. N. Smelyanskiy, D. G. Luchinsky, A. Stefanovska, and P. V. E. McClintock. Inference of a nonlinear stochastic model of the cardiorespiratory interaction. *Physical Review Letters*, 94(9):098101, 2005.

[46] V. N. Smelyanskiy, D. G. Luchinsky, D. A. Timucin, and A. Bandrivskyy. Reconstruction of stochastic nonlinear dynamical models from trajectory measurements. *Physical Review E*, 72(2):026202, 2005.

[47] K. Visscher, M. J. Schnitzer, and S. M. Block. Single kinezin molecules studied with a molecular force clamp. *Nature*, 400:184–189, 1999.

[48] F. Watanabe, H. Konno, and S. Kanemoto. Identification method of stochastic nonlinear dynamics using dynamical phase analysis-application to forsmark data. *Annals of Nuclear Energy*, 31(4):375–397, 2004.

[49] J. Wu, G. Biswas, S. Abdelwahed, and E. Manders. A hybrid control system design and implementation for a three tank testbed. In *Control Applications, 2005 IEEE*, pages 645–650, 2005.

[50] A. Zolghadri, D. Henry, and M. Monsion. Design of nonlinear observers for fault diagnosis: a case study. *Control Engineering Practice*, 4:1535–1544, 1996.